The Thesis Committee for Javier Andres Estrada Santos

Certifies that this is the approved version of the following Thesis:

Lattice-Boltzmann Modeling of Multiphase Flow through Rough Heterogeneously Wet Fractures

APPROVED BY

SUPERVISING COMMITTEE:

Supervisor: _____

Maša Prodanović

_____

Hugh Daigle

Lattice-Boltzmann Modeling of Multiphase Flow through Rough Heterogeneously Wet Fractures

by

Javier Andres Estrada Santos

Thesis

Presented to the Faculty of the Graduate School of

The University of Texas at Austin

in Partial Fulfillment

of the Requirements

for the Degree of

Master of Science in Engineering

The University of Texas at Austin

August 2018

Dedication

To my mother.

Acknowledgments

I would like to thank all of the individuals who have inspired me during my master's degree and made this work possible.

First, I would like to express my sincere gratitude to my supervisor, Dr. Maša Prodanović, for her guidance during these past two years and the many years to come. I thank Dr. Christopher J. Landry for his insights and fruitful discussions about the numerical and geological aspects of this work. I also thank Dr. Hugh Daigle for his valuable revisions that contributed to the improvement of this thesis. Additionally, I would like to acknowledge Honggeun Jo for adding his expertise in statistics, which augmented the analysis performed in this work.

I would like to thank my research group, along with the staff of the Hildebrand Department of Petroleum and Geosystems Engineering, for being welcoming and supportive throughout the course of my degree. Thank you to my friends Dakota Stormer, Jenny Ryu, Andres Gonzalez, Jose Parra, and Lucas and Miguel Mejia, for your informal collaboration, support, and guidance.

Thank you, Dr. Matthew Balhoff, for giving me the opportunity to be your teaching assistant for the reservoir simulation for graduate students class, and for supplying unlimited amounts of coffee. Thank you, professors Marc Hesse, Farzam Javadpour, and Michael Pyrcz for providing me with a strong academic background. Thank you, Josephina Schembre and John Pederson, my mentors from Chevron, for playing a crucial role in my professional growth.

Finally, I would like to thank the rest of my family and friends whom I did not cite explicitly for their love and support.

All of you were an important part of the success of this work, and it has been a

privilege working by your side. Without all of you, none of this would have been possible.

Abstract

Lattice-Boltzmann Modeling of Multiphase Flow through Rough Heterogeneously Wet Fractures

Javier Andres Estrada Santos, M.S.E.

The University of Texas at Austin, 2018

Supervisor: Maša Prodanović

Fractures are widely present in the subsurface, often representing primary channels for fluid flow in low permeability rocks. While fracture surfaces are composed by different minerals and are rough by nature, mathematical models to predict flow properties rarely take in account these heterogeneities. Therefore, the pore-scale mechanisms of flow through fractures are not well understood. Because characterizing multiphase flow phenomena in these geometries has received limited attention, this thesis aims to address this issue, by studying the effect of surface roughness and heterogeneous wettability in immiscible displacement through single fractures.

Since analytical solutions are restricted to simple domains and obtaining data from laboratory experiments is unpractical, a 3D direct simulation approach via the lattice Boltzmann method was selected. This was chosen based on its rigorous kinetic derivation, its ability to simulate immiscible displacement, and its versatile boundary conditions.

To study the effects of surface heterogeneities, synthetic domains exhibiting geometrical mineral arrangements, and self-affine fractures were created to carry out drainage

and imbibition simulations with different input parameters. The relationships of different wetting/non-wetting patterns and surface roughness, with interfacial areas, capillary pressure, and residual fluid saturation were quantified.

It has been shown that there is an effective heterogeneous feature size related to the fracture dimensions that modifies the capillary pressure behavior, and the shape of an invasive fluid front. We further found that for increasingly rough surfaces, there is a linear relation between the residual non-wetting saturation and capillary pressure with the aperture distribution. Thus, the shape, mineral size ratio, and surface roughness can have a significant effect on flow behavior.

The results of this work can be used to better inform field simulations, by providing physically-accurate input parameters to characterize fracture network models, enhanced flow rate predictions for naturally fractured reservoirs can be obtained.

Table of Contents

Glossary

a: fracture aperture

BGK: Bhatnagar-Gross-Krook approximation

G: Geometric factor

LBM: Lattice-Boltzmann method

lu: lattice units

NS: Navier-Sokes equation

NFR: Naturally fractured reservoirs

SC: Shan-Chen model

ϵ**:** Convergence threshold

List of Figures

List of Tables

Chapter 1: Introduction

Natural fractures are ubiquitous in subsurface formations, which are of interest for hydrothermal fluid migration studies, contaminant remediation in aquifers, and oil and gas production. For petroleum reservoirs, it has been shown that 60% of the world's reserves are located in naturally fractured formations [32]. Hence, authors suggest that every hydrocarbon reservoir should be classified as fractured initially, until proven otherwise [64, 65]. In a field, the presence of fractures can be critical for every stage of its development (from exploration, drilling and completions, to reservoir management), due to the special treatment that these require.

Open fractures in the subsurface act as preferred channels for fluid flow, playing a crucial role in the oil and gas industry, because most of the world's hydrocarbon production comes from either natural, or artificially-created fractures. In low permeability reservoirs (unconventional reservoirs or tight formations), fractures act as primary pathways for flow, allowing production from these formations to be profitable. In carbonate reservoirs, natural fractures are key for extracting hydrocarbons out of the tight rock matrix (this mechanism is how most of the world's oil is produced). Nonetheless, flow paths in fractures could be blocked due to fine grain filling, or product of diagenetic processes (such as cementation) [50, 68]. Closed fractures act as permeability deterrents. For these reasons, the prediction of how fluids travel through fractures is a topic of increasing interest.

Fluid flow through fractures is mainly controlled by the separation of the solid surfaces that bound the void space (aperture field) [25]. Nevertheless, other factors including surface roughness, mineral composition, permeability of the fracture surface, and fracture network connectivity have an impact as well. It is important to understand how these variables affect the flow of fluids through a reservoir to interpret well measurements properly,

calculate reserves accurately, and craft precise predictive models.

Commonly, fracture surfaces are composed by a variety of minerals that possess a distinct affinity for a fluid present in the reservoir [17]. To make accurate predictions of the flow properties in a reservoir, it is necessary to understand how the fluid behaves in the presence of the different mineralogies of the solid surfaces. Furthermore, fractures in the subsurface exhibit surface roughness [9], which adds additional complexity for carrying out multiphase flow predictions. Surface roughness modifies the local fracture aperture and could cause different complications for flow and could modify the capillary pressure curves. Typically, models that are used to predict the flow capabilities of a fracture, do not take in account these last two factors. Nevertheless, it has been shown that they have a relevant role in primary hydrocarbon production and enhanced oil recovery [22].

Heterogeneous wettability and surface roughness modify the flow patterns by increasing the tortuousity of the fluid paths [94], trapping fluid [22], and providing preferred channels for flow [75]. Presently, there is not enough pore scale studies to fully understand how flow processes act with the different heterogeneities existing in natural fractures. Hence, a understanding on how wettability and roughness affect flow through fracture at the pore scale is relevant.

Conventionally, the approach used to describe flow in porous media is to take a representative elementary volume (volume over which a measured property will represent the whole) [6], and solve the domain as a continuum. For flow of multiple phases, the saturations of each fluid are used to draw flow predictions, this results in a Darcy based, relative permeability approach.

There is a number of analytical models that describe the behavior of fluids contacting surfaces with different patterns [12, 100]. Nevertheless, they are restricted to very simple arrangements, so they fail to predict the behavior on the surfaces that could be encountered in a reservoir. Cassie [12] proposed a relationship to calculate an effective

contact angle on a flat surface with two components (labeled 1 and 2):

$$cos\theta_{eff} = f_1 cos\theta_1 + (1 - f_1) cos\theta_2, \tag{1.1}$$

where θ_{eff} stands for the calculated 'effective' contact angle of the system, θ_1 and θ_2 represent the contact angle of each component, and f the areal fraction covered by them. This expression assumes that the most relevant parameter is the areal fraction occupied by a certain mineral, an obvious limitation is that it can only account for two different materials. Other studies have suggested that the contact angle is shaped by the interactions that occur at the triple-point [56]. Further work studied the validity of the Cassie equation, but limited to a single droplet [24, 37, 46, 47, 106]. Another difficulty that is faced while modeling these processes, is the variable wettability of the minerals in presence of reservoir fluids [97]; it has been shown that a single system can exhibit contact angles raging from 0 to 90 degrees [36].

On the other hand, Wenzel [100] proposed the following analytical solution to account for surface roughness:

$$cos\theta_{eff} = r cos\theta, \tag{1.2}$$

where r represents the fraction of the surface that is in contact with the fluid calculated as follows:

$$r = \frac{L_r}{L_f}, \tag{1.3}$$

where L_r represents the length of the rough surface that is in contact with the fluid and L_f the flat projection of this [103].

Wolansky et al. [104] mathematically proved that the Wenzel equation provides accurate results when the size of the drop is indefinetely large compared to the scale of the roughness. Shibuichi et al. [88] experimentally showed that in a hydrophilic surface Equation 1.2 yields in good approximations.

Typically, multiphase flow through fractures is modeled using idealized solutions (flow through parallel plates, or straight relative permeability curves), where the complexities mentioned above are not taken into account [80]. It has been demonstrated, that the predictions made with these can vary by orders of magnitude [95], and they provide an oversimplified view of the complex multiphase flow displacement. New imaging techniques, ability to build better physical models, more powerful computers, and better algorithms have been responsible of an better understanding of the complexities of flow though fractures. Further studies have shown that the multiphase displacement, specifically phase trapping through fractures, resembles porous media matrix behavior [76, 78], unlike previous work suggested.

While laboratory experiments enhance the understanding of multiphase flow, they fail to capture the microscopic effects locally that arise due the presence of heterogeneities at the microscopic scale. So a common practice to recreate fracture surfaces digitally (from faults spanning km., to microfractures) is to characterizing them using fractal dimensions and a spatial correlation component of the bounding surfaces [45].

For this study, we selected the lattice-Boltzmann method (LBM) based on its ability to simulate flow through complex geometries, its highly parallelizable algorithm, and its kinetic theory consistency. To further investigate multiphase flow, the Shan-Chen (SC) LBM was chosen based on its capability to simulate multiple phases that honor the properties of an oil-brine system, and its capacities of handling complex boundary conditions. Other options include quasi-static level set methods [40, 98] (although these do not take in account viscous forces), or volume of fluid methods (which prove more complicated to implement heterogeneous wetting surfaces) [82].

Previously, the SC LBM has been used to study flow through porous matrix [72]. In the context of fractured media, Dou et al. [22] showed how homogeneous rough fractures with different contact angles impact the unsteady-state capillary pressure curves. Landry et

al. [49] studied how the heterogeneous composition of a bead pack adversely affected the relative permeability compared with homogeneous-wet states. To our knowledge, this work provides the first effort to characterize heterogeneous, roughly-composed fracture surfaces with a direct simulation approach. Comprehensive validation tests were done to assure that the model was able to simulate the required processes.

In Chapter 2 a brief introduction to the relevant petrophysical concepts that describe multiphase in porous media is presented. In Chapter 3 the relevant literature outlining the geologic, mathematical, and petrophysical background of this work is cited. Chapter 4 provides the reader with a derivation of the mathematical model utilized in the simulations for this work. The validation of the model with analytical solutions follows in Chapter 5. Subsequently, in Chapter 6 the results of the simulations are shown and analyzed.

The primary goal of this thesis is to demonstrate that a pore-scale understanding of how fluids travel through realistic fractures can provide insight on larger scales.

Chapter 2: Multiphase phenomena and fluid-rock interaction

Multiphase phenomena and interactions between fluids and rock surfaces occur regularly in natural systems and industrial applications. These events take place when two or more immiscible fluids (incapable of being mixed) share an interface. Below, concepts relevant to this work are defined and briefly explained.

2.1 Interfacial tension

Whenever two immiscible fluids are adjacent to each other, an interface forms as the result of the molecular unbalance of forces (Figure 2.1a). This causes the formation of a membrane-like layer along the surface where the two fluids contact, which is typically a few molecular diameters in thickness.

2.2 Wettability

Wettability is the relative affinity of a fluid to a solid surface in presence of other immiscible fluids. In a porous system, the pore surfaces are composed by a variety of

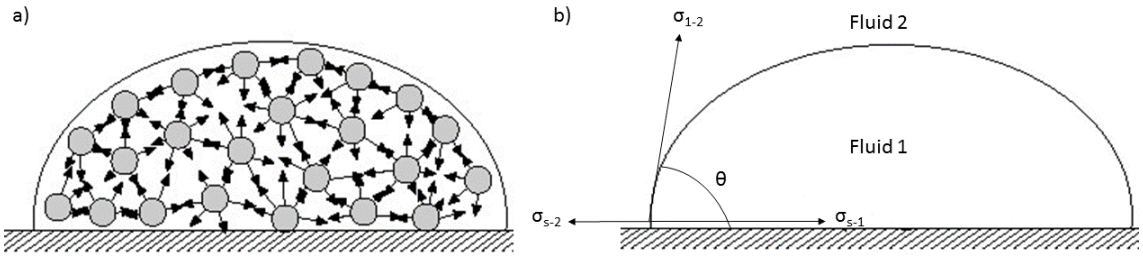

Figure 2.1: a) Molecules within the liquid droplet experience interactions in all directions, the force imbalance at the surface results in an interfacial tension. b) Interfacial tensions and contact angle between fluid 1 (denser), fluid 2 (non-wetting), and a solid surface.

minerals that have a distinct preference for one of the fluids present in the medium, or to its suspended or dissolved constituents [21]. The fluid that preferentially adheres to the surface is known as the wetting fluid. When an immiscible fluid is displacing another in a tube, a meniscus appears. The fluid for which the contact angle (between the tube and the meniscus) is smaller than $\frac{\pi}{2}$ is regarded as the wetting fluid.

In a rock/oil/brine system, wettability accounts for the preference of the rock to be in contact with oil or water. This preference is shaped by the surface mineralogy, the fluid composition, the shape of the pores, and the history of previous immiscible displacements. In a homogeneously water-wet rock, the water phase prefers to inhabit the smaller pores, and the corners of larger pores, to contact most of the solid surface available.

Wettability is the dominant parameter in the microscopic distribution of oil and water in the pores, the shape of the capillary pressure curves, and the amount and location of the residual volume of oil in a reservoir. Although the average or dominant wettability is commonly reported, the wettability of a natural porous medium is non-uniform. Therefore some authors utilize heterogeneous distributions to define the wettability of a porous medium [20].

The wettability of a system can be quantified experimentally by a) measuring the angle (Figure 2.1b) that is formed between the solid surface and the interface between two fluids [3] b) core scale laboratory experiments [2] and the U.S. Bureau of Mines (USBM) or by c) pore-scale measurements [4, 17].

The interfacial tensions (specific free surface energies) and the contact angle of a sessile drop on a flat surface are related to the contact angle by the Young-Dupre equation:

$$cos\theta = \frac{\sigma_{1-s} - \sigma_{2-s}}{\sigma_{1-2}}, \tag{2.1}$$

where σ_{1-s} is the solid-fluid 1 interfacial tension, σ_{2-s} is the fluid 2-solid interfacial tension, and σ_{1-2} is the fluid 1-fluid 2 interfacial tension. This equation ignores the three-phase

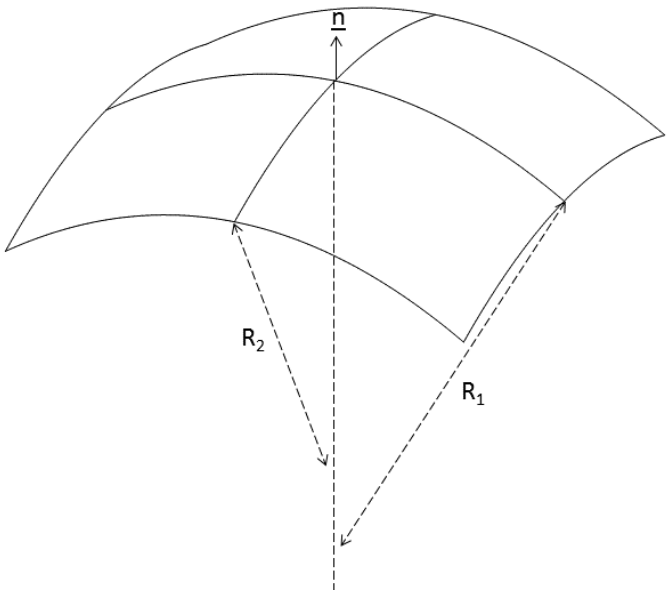

Figure 2.2: Geometry of the interfacial area, parametrized by the two perpendicular radii of curvature R_1 and R_2. The normal vector $\underline{n}$ points towards he wetting fluid, located on the concave side.

molecular interactions at the contact line between the solid, and the two fluid phases.

2.3 Capillary pressure

The capillary pressure arises from the discontinuity of pressure between two neighboring immiscible fluids. This pressure difference leads the shared interface to curve (Figure 2.2). The fluid with the higher pressure will be on the concave side. The capillary pressure can be calculated using the Young-Laplace equation:

$$P_c = P_{nw} - P_w = \sigma c = \sigma\left(\frac{1}{R_1} + \frac{1}{R_2}\right), \tag{2.2}$$

where the subscripts nw and w denote the wetting and non-wetting fluid, c represents the curvature of the interface (which is mathematically equal to twice the mean curvature of an interface), composed by the principal radii R_1 and R_2, and σ stands for the interfacial tension between the fluid pair.

For a capillary tube, Washburn [99] proposed the following solution to the equation presented above:

$$P_c = \frac{2\sigma cos\theta}{r}, \tag{2.3}$$

where r represents the radius of the tube.

2.3.1 Immiscible displacement through porous media

There are two main types of immiscible displacement processes: drainage and imbibition.

In imbibition, the wetting phase displaces the non-wetting one, if the rock is completely saturated with non-wetting fluid, a spontaneous imbibition process can happen. Drainage is the inverse process, and in order for the non-wetting phase to start invading the medium, overcoming an entry pressure is necessary (P_e). This is a function of the largest pore structure connected to the non-wetting phase (given by Equation 2.3). A diagram showing the capillary pressure-saturation curves of these processes is shown in Figure 2.3.

As shown by Hassanizadeh et al. [33], the frequently utilized relationship of capillary pressure $P_c = P_c(S_w)$ is an empirical approach that does not take into account all effects and processes that happen at the microscale. They observed that capillary pressure is also a function of the interfacial area between fluids, which is able to better explain hysteresis in capillary pressure-saturation curves. This is relevant because other important phenomena, like mass transfer between phases, is proportional to the interfacial area between liquids, and it has been shown [38] that is heavily dependent on the wettability of the solid. Knowing the interface distribution and interfacial areas is critical to describe the capillary pressure-saturation relationship of a porous medium, and to explain the hysteresis in the curves. Several studies have shown that capillary pressure depends on several factors, including the history of imbibition and drainage cycles [84], injection rate [44], among others. There have been published attempts to quantify the effect of different interfacial

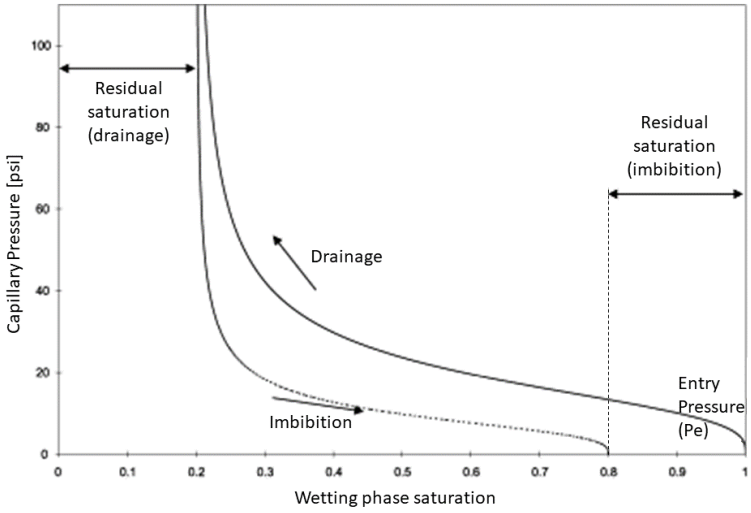

Figure 2.3: Immiscible displacements: drainage and imbibition capillary pressure curves. The residual (or irreducible) saturation of a fluid corresponds to the volume of wetting fluid that is not able to flow due to rock-fluid and fluid-fluid forces, under fixed thermodynamic conditions.

configurations [13].

2.3.1.1 Hysteresis

Hysteresis is the difference of the drainage and imbibition capillary pressure curves. This means that these two flow processes are non-reversible. Figure 2.3 exhibits a bigger change of the wetting phase saturation saturation compared to the one on the imbibition process:

$$\left(\frac{dS_{nw}}{dP_c}\right)_{drainage} > \left(\frac{dS_{nw}}{dP_c}\right)_{imbibition}. \tag{2.4}$$

There are a number of factors that cause this phenomenon like contact angle hysteresis [41], bistability of an interface in a non-uniform medium (Figure 2.4), less interface configurations , fluid trapping, among others.

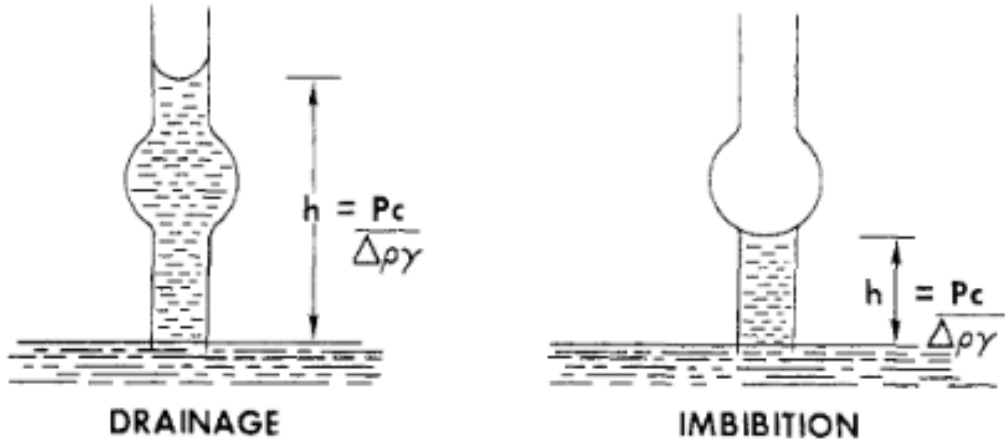

Figure 2.4: Bistability of an interface in a nonuniform tube. The liquid level depends on its initial condition, when the tube is slowly raised the interface travels through the bulbous region spontaneously. Likewise, when the tube is lowered the liquid will spontaneously imbibe into the bulb, at a different pressure than in the drainage process. This experiment shows that many stable configurations are possible in a non-uniform porous medium (from [63]).

2.4 Flow through fractures

Open fractures in the subsurface represent primary channels for flow in low permeability rocks. Interconnected open fractures do not contribute with storage capacity, but greatly enhance the hydraulic conductivity of a reservoir.

In a water-wet reservoir, the water traveling through the fracture that contacts the hydrocarbon saturated zone, imbibes into the matrix, expelling the oil into the fracture system (Figure 2.5). The aperture distribution is the most relevant parameter that controls flow. Nevertheless, the fracture surface composition also affects the behavior of fluids. Most of the times, the displacement processes through fractures are modeled as piston-like displacements in between two parallel plates. However, a number of recent publications [22, 66, 76, 96] show that flow through natural fractures exhibit a behavior that resembles porous media displacement, featuring hysteresis and non trivial capillary pressure-saturation functions.

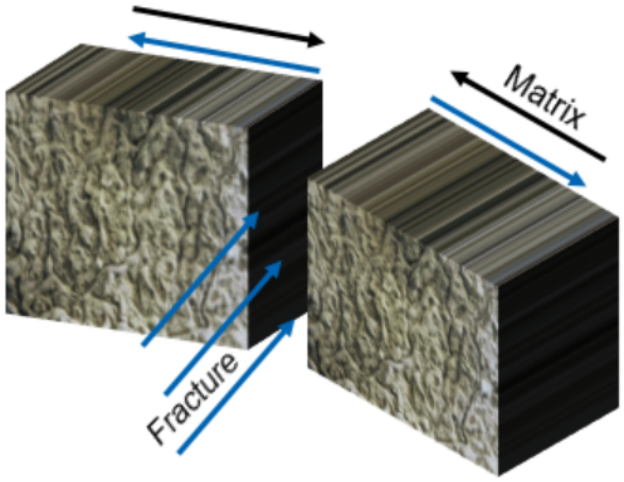

Figure 2.5: Water being imbibed to the oil satured matrix. The oil is expelled out to the fracture network and can be produced.

2.5 Dimensionless numbers

The dimensionless numbers are used to normalize problems at different scales, and to assess the relative impact of forces in specific problems. The following dimensionless numbers are used throughout this work to describe the impact of a given force:

2.5.1 Reynolds number

The Reynolds number provides a ratio between two hydrodynamic time scales, and it is given by the following equation:

$$Re = \frac{\rho \nu L}{\mu}, \tag{2.5}$$

where ρ represents the fluid density and L the characteristic problem length. Lee et al. [51] studied the effect of different Reynolds numbers in multiphase flow through rough fractures experimentally. They found that in Reynolds numbers regimes equal to 1, the fluid path and

speed where strongly affected by wettability. Whereas with a Reynolds number equal to 60, wettability effects become insignificant due to the inertial pressure (square of the flow velocity).

2.5.2 Capillary number

When fracture apertures become smaller that 1 millimeter, capillary forces start becoming dominant for immiscible displacements. This can be quantified as follows [48]:

$$C_a = \frac{\nu\mu}{\sigma}, \tag{2.6}$$

where ν stands for the system's characteristic velocity and μ for the fluid viscosity. This number provides a measure of the dominance of viscous forces over capillary forces. For numbers smaller than 10^{-4} the flow is said to be dominated by capillary effects.

2.5.3 Mobility ratio

The mobility ratio is defined as the ability of the displacing phase to travel through the system divided by the one of the displaced phase:

$$M = \frac{\mu_{nw}}{\mu_w}\frac{k_{r_w}}{k_{r_{nw}}}, \tag{2.7}$$

the dominance of the viscous or capillary forces in immiscible displacement through porous media can be quantified with these last numbers [53]. Lenormand et al. [54] investigated immiscible displacement in micromodels (quasi-2D systems) with different capillary numbers and mobility ratios (Figure 2.6), finding that instabilities in flow lead to poor recoveries.

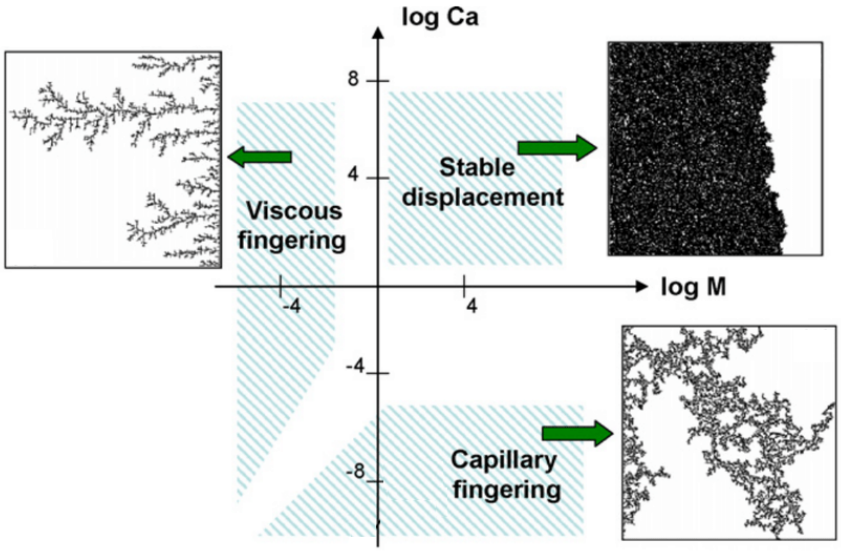

Figure 2.6: Representation of Lenormand's [52] phase diagram showing three different flow regimes (Modified from [89]).

2.5.4 Bond number

The Bond number characterizes the relative strength of surface tension in the presence of a gravitational field, and it is expressed as follows:

$$Bo = \frac{\Delta \rho g r^2}{\sigma}, \tag{2.8}$$

where g represents the gravitational acceleration and r the length scale (typically, the radius of droplet or bubble). Very small numbers mean that the impact of the gravitational force is negligible, and that the shape of a fluid body is going to be dominated by the tension between the fluid phases.

Chapter 3: Literature review

Fractures in subsurface formations are discontinuities created by brittle failure due to stress responses. Geologically, there at two main fracture types by their genesis, joints and faults.

Joints form in tension, where fracture walls pull away of each other, without any shearing displacement. Joints can greatly enhanced the permeability of reservoirs globally [64]. Faults form in compression, with shearing displacement. They can enhance or block fluid flow (locally), depending on its composition.

Fractures can be present in every lithology, and can span a wide range of scales; from micrometers to kilometers [11, 27]. While subsurface stress will tend to close fractures, these may remain open due to the shifts along the shear direction, roughness, erosion, dissolution, and elevated fluid pressures. Open fractures are relevant for industrial applications because they could control the dispersion of pollutants in the subsurface, they affect the stability of man-made subsurface structures (like wells and excavations), and they are important for heat transfer in geothermal fluids.

3.1 Naturally fracture reservoirs

A naturally fractured reservoir (NFR) is a reservoir which production performance is significantly affected by the presence of fractures. These reservoirs have two main elements, a porous matrix and a fracture network. Naturally fractured reservoirs (NFR) can be classified by the contribution of the rock fractures to storage and conductivity, as shown by Nelson [65] in Table 3.1. Throughout this work, we are focused in modeling single fractures in type 2 NFRs, where the fractures represent the main flow channels compared

Table 3.1: Naturally fractured reservoirs classification by Nelson. (Modified from [65])

Type	Definition	Locations
1	Fractures provide essential porosity and permeability	Amal, Libya Edison, California Basement fields, Kansas
2	Fractures provide essential permeability	Agha Jari, Iran Haft Kel, Iran Sooner trend, Oklahoma Spraberry trend area, Texas
3	Fractures provide a permeability enhancement	Kirkuk, Iraq Dukhan, Qatar Cottonwood Creek, Wyoming Lacq, France

to the matrix.

NFRs are not always easy to identify. Some signals that a reservoir could be naturally fracture are: mud losses or bit drops during drilling operations, peculiar production behavior (interference o higher well productivities), among others.

During the first stage of the primary production in a NFR, the oil contained inside the fractures near the wellbore, and neighboring matrix is produced. As production continues, the oil initially stored in the fractures is depleted, and most of the reserves remain stored in the rock matrix. Water injection processes are commonly applied in water-wet reservoirs, where water can spontaneously imbibe into the matrix, displacing the oil into the fracture network. However, when the matrix rock is oil-wet or mixed-wet the amount of displaced oil is less significant. For this cases, a surfactant injection process can improve the oil recovery by altering the wettability of the host rock and/or lowering the interfacial tension between the fluids. For the former case, a positive capillary pressure is achieved and imbibition can take place [55], for the latter, the buoyancy forces dominate due to the low capillary pressures [5].

3.2 Single fractures

Studying conductive fractures in the subsurface is specially challenging due to sampling difficulties. First, fractures tend to be vertical and widely spaced (compared to a well diameter), so a vertical well is only able to capture a limited amount of them. Also, fractures have heterogeneities at long scales, so these attributes remain elusive in the data obtained from a well [58]. Outcrops are also a common source of information to study the fracture characteristics of a certain formation, because outcrops contain a larger sampling space. However, outcrops also could be misleading due to weathering and uplift induced fractures that were not in the formation's original setting.

In this work, we look to investigate the relevant factors that affect the flow of multiple fluid phases through individual fractures. For instance, diagenetic processes (chemical and mechanical changes in the sediments after deposition) can modify the void space geometry in fractures by cement precipitation, lining the solid walls of bridging the fracture completely [50]. Nevertheless, it can also have the opposite effect, fluids flowing through fractures could also react with the rock, dissolving the solid walls and enlarging their apertures [19, 31]. These changes yield in a heterogeneous fracture aperture field.

Tokan-Lawal [93] proposed a classification based on fracture filling and morphology, shown in Table 3.2. In this work we are interested in studying open and mineral-filled fractures. Another important characteristic in flow through fractures is aperture. Studies have shown that the kinematic aperture of a single formation could span several orders of magnitude [59], and that could follow a power law (Figure 3.1). So the average size of the fractures in a formation is not well defined.

3.2.1 Single phase flow

Conventionally, predictions for flow through a single fracture have relied on the fact that a fracture can be well represented by a pair of smooth, homogeneous, parallel plates

Table 3.2: Single fracture classification by pore space morphology

Type	Description
Open fractures	Uncemented without secondary mineralization. They significantly enhance the permeability of a formation.
Deformed fractures	Frictional sliding (slickensides, these decrease the permeability of the rock), or Grinding (deformation bands, could act as conduits)
Mineral-filled fractures	These could be completely or partially filled with cements
Vuggy fractures	Resultant of dissolution from flow of acid waters

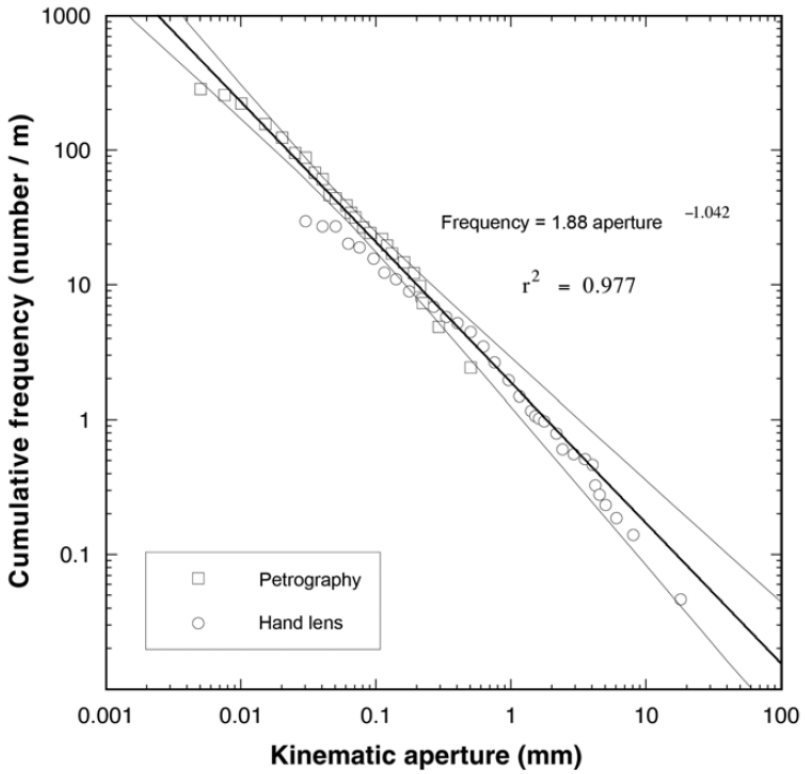

Figure 3.1: Fractures commonly have apertures that follow a power law distribution. This plot shows data from an a Marble Falls Limestone outcrop measured with a hand-lens and a microscope. (From [59]).

(Figure 3.2). This is done due to the simplicity of deriving a solution for flow through this geometry. The analytical solution of the Navier-Stokes equation for single-phase flow through a smooth-walled fracture with a no-slip condition is provided by the cubic law:

$$q = -\frac{a^3 w}{12\mu}\frac{\Delta p}{\Delta z}, \tag{3.1}$$

where a stands for the fracture aperture, w for the fracture width, $\frac{\Delta p}{\Delta z}$ for the pressure gradient, and μ for the fluid viscosity. This expression is known as the slit analog of the Hagen-Poiseuille equation. In this model it is assumed that the fracture height (Δz) and the fracture width (w) are much larger than the aperture (a), so end effects are not taken into account. If we relate this single fracture flow equation with Darcy's Law [15], the following relation to calculate permeability is obtained:

$$k = \frac{a^2}{12}, \tag{3.2}$$

where if the intrinsic porosity of the fracture (ϕ_{if}) is known, it can be included as:

$$k = \frac{a^2}{12}\phi_{if}. \tag{3.3}$$

From this equation, we can see that the fracture aperture is the dominant factor for fluid conductivity in this geometry. However, assigning a value for this is represents a non-trivial task, partly due to the following factors: natural fractures are heterogeneous entities and the distance between its two bounding solid plates varies greatly, there is no clear definition of how to calculate the fracture aperture (Figure 3.3), and open fractures could be partially filled with cement which creates an additional complication for flow channels.

There is a considerable amount of correlations proposed based on the cubic law (Equation 3.1) to account for more realistic fracture geometries [10, 25, 70, 102]. Tokan-

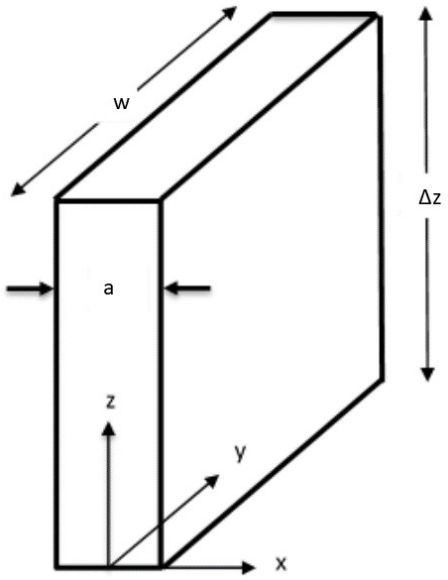

Figure 3.2: Parallel plate model representing a single fracture.

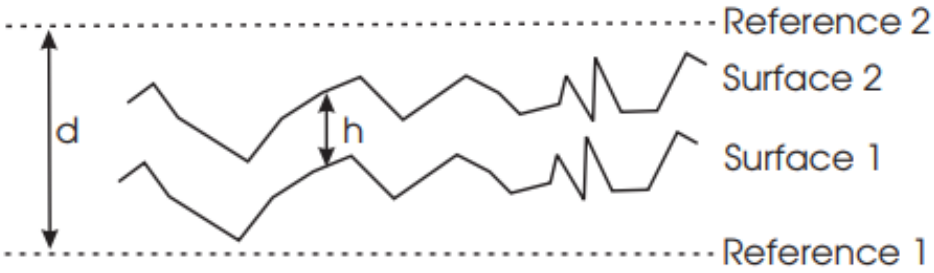

Figure 3.3: Two rough fracture surfaces separated by an aperture h, the reference planes are separated by a distance d. (from [107]).

Lawal et al. [95] showed that some of these could span several orders of magnitude among them, and compared with the result of a direct simulation performed on an microtomography fracture image (Figure 3.4b). Further, models [107] suggest that the cubic law could be enhanced by taking in account the variability in the aperture field locally (known as the Reynolds equation).

3.2.2 Multiphase flow

There are no widely accepted correlations for calculating relative permeability and fluid saturations in a fracture. If the parallel plate model is extended for multiphase flow, it yields in a straight relative permeability model; where the fluids occupy a fraction of the fracture aperture and travel side by side, so the relative permeability of each is equal to their individual saturations:

$$K_{r_i} = S_i \qquad i = \{o, w, g\}. \tag{3.4}$$

In 1966, Romm [85] presented a experimental study where he provided evidence to support that the relative permeability of a fracture was only function of the saturation of each fluid (linear dependency). Later, Pruess and Tsang [80] conducted a simulation study, where their results showed that the wetting fluid has a significant advantage for flow, which impacts the relative permeability curve behavior, and the relations are no longer linear. Further studies concluded that the relative permeability of a fracture behaves in a similar fashion to a porous medium [75, 76], being impacted by several different factors, like the spatial configuration of the phases along the void space of the fracture, and by the trapped phases in low aperture/rougher areas [95]. As suggested by several authors [1, 76], the complicated morphology of a single fracture greatly affects flow and cannot be described through simple equations.

Another open question is how fractures interact in presence of a permeable matrix. Prodanovic et al. [79] investigated the case where the fracture surface was composed by a porous material using the level-set method. They found that the non-wetting phase trapping was highly sensitive to the direction of displacement.

3.2.3 Fracture topology characterization

A complication that the modeler faces while working with natural fractures, is how to deal with surface roughness. It is commonly accepted that the roughness acts as a flow barrier. Nevertheless, roughness can also channelize flow [83] by creating preferred paths, and considerably reducing the relative permeability of the wetting phase.

Attempts to parametrize the natural fracture surfaces (using profilometer and microtomography images) for further studies have been made with the goal of capturing the morphology of the walls, providing more realistic models. Studies have shown that roughness has a self-affine fractal property independently of their scale, morphology or genesis [9, 10]. There is on-going discussion on the measurements techniques, profilometer measurements [69] are done on a surface at the time, so the fracture has to be opened, and might lose some of its features. Microtomography images [101] are limited in resolution and prone to artifacts and noise.

Leaving these complications aside, fracture roughness can be quantified through a fractal dimension (D_f) [57], which measures the topological complexity of an object (0 for a point, 1 for a curve, 2 for a surface), where a related measure is the Hurst exponent [30]. Furthermore, fractures are spatially correlated, though it is not a straightforward parameter to measure: Brown [10] presented a model to describe the fracture surfaces that included a mismatch length term that defined the scale on which the surfaces were correlated. Later, Ogilvie et al. [67] improved the model by adding a transition length parameter to account for the speed of the wavelength match (the correlation of the Fourier components at a certain wave length), and successfully parametrized and recreated several natural fractures in different lithologies. Dou [23] investigated the effect of fracture roughness in solute transport, finding that most of the concentration front travels through the central aperture region, leaving the area close to the solid surface (where the size of this area is function of the Reynolds number) not contributing to the transport of solutes due to roughness.

3.2.4 Fracture aperture

There are still open questions regarding how to calculate the fracture aperture from a given dataset. Some studies suggest that the definition of aperture should rely on the processes that would like to be study (single-phase flow, multiphase flow, reactive flows, transport of components). For example, a study [61] shows that the flow is sensitive the the orientation of the heterogeneities, exhibiting that for a fracture with the same mean aperture, flow could be enhanced or deteriorated compared to an analytical solution. Other studies have shown that the local cubic law solution of the Reynolds equation can describe flow through rough fractures. Although, a local approach could be a starting-point for solving these problems, it is unclear on how the local fracture aperture should be used/measured. As a first approach, aperture can be measured vertically in all directions. Nonetheless, in regions with a preferred dipping direction, the measured aperture would not be representative of the open area for flow. Ge [28] suggests to calculate the aperture using the axis of the flow direction, although this proves conflictive in fractal domains, because normals change directions at a given point depending on the resolution. Another option is using a center sphere approach, growing a sphere until it touches both ends; nonetheless, this would not capture the area open for flow within the crevasses of the solid surface. Finally, Oron and Bekovitz [70] showed that the aperture should be measured over a certain length (effective area) and not at every point.

3.3 Concluding remarks

There is not a single accepted model to account for the natural complexities in fractures. Thus to better understand the flow through these intricate domains, we selected a 3D direct modeling approach to assess the impact of the surface heterogeneities in drainage and imbibition simulations. The numerical method that we used will be introduced in the next chapter.

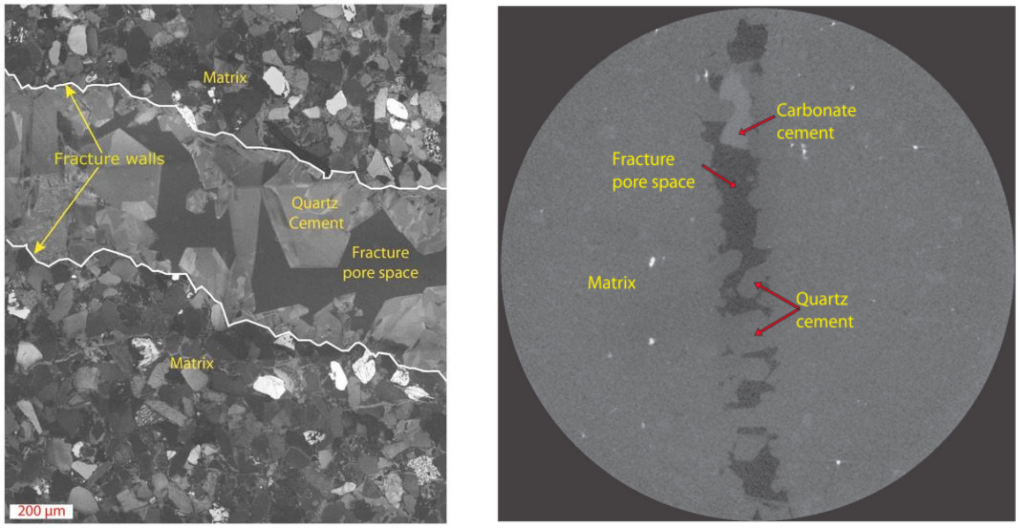

(a) Scanning electron microscopy (SEM) image.

(b) Slice of a microtomography (μct) image. The diameter of the sample is 4.2 [mm].

Figure 3.4: Digital images from a Travis Peak sandstone fracture. This is partly cemented with quartz bridging across the fracture, and euhedral quartz cement lining the walls [95].

Chapter 4: The lattice-Boltzmann method

The lattice-Boltzmann method (LBM) was first proposed [60] as an alternative to the lattice-gas automaton [105] to study hydrodynamic properties with the Boltzmann equation. To this day, the LBM has developed into a competent computational fluid dynamics (CFD) tool that is able to simulate multiphase, thermal, and reactive flows, among others. The kinetic nature of method derivation aids in the coupling of other physical phenomena describable at the molecular level.

The LBM stands out in problems where solving the Navier-Stokes (NS) equation becomes troublesome, like during flow through complex geometries, turbulent flow, large Knudsen number flow, etc. The simulation does not require solving complex operations (unlike solving the Poisson equation), so the implementation is relatively simple and easily parallelized.

The LBM relies on probability density functions to represent particle movement, where the domain is divided with nodes, which host particles that propagate and interact in their neighborhood. Unlike molecular dynamics (MD) simulations, the LBM does not track individual molecules, but the bulk of them (probability density functions). From this, it is possible to calculate the macroscopic variables (i.e. density and velocity). Even for simple cases (2 dimensions, 6 discrete velocities), the simulation is able to accurately match the NS equation.

4.1 LBM derivation

The LBM model is based on the Boltzmann equation:

$$\frac{\partial f}{\partial t} + v\frac{\partial f}{\partial \underline{x}} + F\frac{\partial f}{\partial v} = \left.\frac{\partial f}{\partial t}\right|_{coll}, \tag{4.1}$$

where f is the distribution function of molecules, t the time, v the velocity, F an external force and $\frac{\partial f}{\partial t}\big|_{coll}$ the change of the distribution due to molecular collisions. This equations can be seen as an advection equation, where the distribution function is being advected with a velocity v, and the third therm represents the forces impacting the velocity, and the last term (local redistribution of particles) act as a source.

The complexities that arise due the use of the last term (Boltzmann's operator is a double integral over the velocity space) can be avoided using a mean-free-path approach [7], replacing the rate of distribution change by a relaxation term:

$$\left.\frac{\partial f}{\partial t}\right|_{coll} = \frac{f - f^{eq}}{\tau}, \tag{4.2}$$

where f_{eq} is the equilibrium particle distribution function, and τ is a constant called relaxation time, which physically represents the time of the density function to reach equilibrium.

4.2 The Shan-Chen multicomponent model

For this work, we chose the Shan-Chen (SC) multiphase model [86, 87] with the Bhatnagar-Gross-Krook (BGK) single relaxation time approximation [7], because is able to honor the behavior of a two fluid system, it can handle density and viscosity ratios (they have to be close to the unity for numerical stability, although there are pseudopotential implementations that claim they can achieve ratio ratios up to 500 [56]), and it is able to

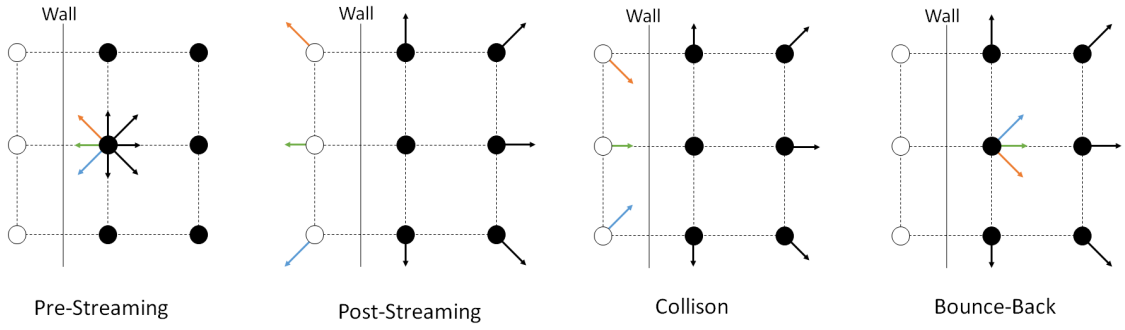

Figure 4.1: The four stages of the lattice-Boltzmann method algorithm.

simulate different wetting conditions.

By discretizing the Boltzmann equation (Equation 4.1) in velocity space, physical space, and time, we are able to derive the lattice-Boltzmann equation:

$$\overbrace{f_{\sigma,i}(x,t) - f_{\sigma,i}(x + e_i\Delta t, t + \Delta t)}^{\text{Streaming}} = \underbrace{\frac{1}{\tau}(f_{\sigma,i}(x,t) - f^{eq}_{\sigma,i}(x,t))}_{\text{Collision}}. \tag{4.3}$$

To simulate a binary fluid flow system, the SC model utilizes two particle distribution functions, that honor the Equation 4.3, and follow the iterative process shown by Figure 4.1. The subscript σ stands for each of the fluids (wetting/non-wetting), the index i refers to the associated discrete velocity direction (Figure 4.2), x to the location of the node on the lattice, and t is the time. The relaxation time represents the rate of particle collision, which is related to the kinematic viscosity by $\nu = c_s^2(\tau - 0.5)$, where c_s is the speed of sound of the lattice or propagation speed equivalent to $c_s = c/3$, and c (discrete lattice speed unit) is calculated as $c = \Delta t/\Delta x$.

The streaming side represents the passing of particles to their respective neighboring node at each discrete velocity (Figure 4.2), while the collision term refers to a relaxation towards local equilibrium given by the following relation for the 3 dimension 19 direction

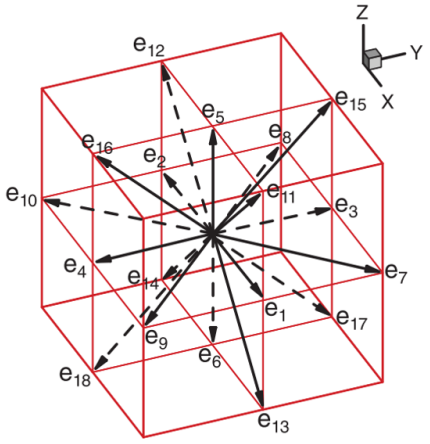

Figure 4.2: D3Q19 discrete velocity model, where D is the space dimension and Q the number of discrete velocity vectors (Modified from [34]).

case (D3Q19):

$$f_i^{eq}(x,t) = w_i\rho\left[1 + \frac{e_i u^{eq}}{c_s^2} + \frac{(e_i u^{eq})^2}{2c_s^4} - \frac{u^{eq2}}{2c_s^2}\right], \tag{4.4}$$

w_i stands for the weight at each velocity, ρ and u^{eq} are the density and macroscopic velocity in $f_i^{\sigma}(x,t)$ respectively. The discrete velocities for the D3Q19 model are defined as follows:

$$[e_0, e_1, e_2, e_3, e_4, e_5, e_6, e_7, e_8, e_9, e_{10}, e_{11}, e_{12}, e_{13}, e_{14}, e_{15}, e_{16}, e_{17}, e_{18}]$$

$$= c\begin{bmatrix} 0 & 1 & -1 & 0 & 0 & 0 & 0 & 1 & 1 & -1 & -1 & 1 & -1 & 1 & -1 & 0 & 0 & 0 & 0 \\ 0 & 0 & 0 & 1 & -1 & 0 & 0 & 1 & -1 & 1 & -1 & 0 & 0 & 0 & 0 & 1 & 1 & -1 & -1 \\ 0 & 0 & 0 & 0 & 0 & 1 & -1 & 0 & 0 & 0 & 0 & 1 & 1 & -1 & -1 & 1 & -1 & 1 & -1 \end{bmatrix}$$

The density if obtained by $\rho = \sum_i f_i$ and the macroscopic velocity u_σ^{eq} can be calculated by [86]:

$$u_\sigma^{eq} = u' + \frac{\tau_\sigma F_\sigma}{\rho_\sigma}, \tag{4.5}$$

where u' is the velocity calculated from the distribution function prior to the collision step and F_σ is the force acting on the component that includes a fluid cohesion and solid adhe-

sion.

$$F_\sigma = F_{co,\sigma} + F_{ads,\sigma}. \tag{4.6}$$

4.2.1 Fluid-fluid interaction

To simulate a binary fluid system (wetting and non-wetting), each fluid is assigned with its own particle distribution function on every node of the lattice. These functions interact by a cohesive force represented by:

$$F_{co,\sigma}(x,t) = -G_c \rho_\sigma(x,t) \sum_i w_i \rho_{\overline{\sigma}}(x + e_i \Delta t, t) e_i, \tag{4.7}$$

where ρ_σ and $\rho_{\overline{\sigma}}$ represent the different fluids and G_c is the interparticle force parameter.

4.2.2 Fluid-solid interaction

The force that the solid wall exerts on the fluid is represented by:

$$F_{ads,\sigma}(x,t) = -G_{ads,\sigma} \rho_\sigma(x,t) \sum_i w_i e_i \cdot s(x + e_i \Delta t, t), \tag{4.8}$$

In here s is a Boolean function that is equal to 1 for a solid (bounce back) node and to 0 for fluid node. G_{ads} controls the interaction strength between the fluids and solid walls.

4.3 Boundary conditions

One of the most attractive features of the LBM is the ability to specify complex boundary conditions in a straightforward manner. Typically, an LBM domain consists of the following pieces: 1) fluid nodes, 2) solid nodes, and 3) boundary nodes. The first ones are where the lattice-Boltzmann equation is solved, the second are used for computational efficiency, and the third are the link between the first two. These can take the following properties:

4.3.1 Infinite (periodic)

These are intended to simulate a repetitive flow pattern, while saving computational resources. The flow that leaves one side of the domain, is conducted to its opposite side. To implement this, the streamed population on a side is given by the ones leaving the opposite side of the domain.

4.3.2 Bounce-back

During the streaming part of the algorithm, if a particle meets a solid node, it will be mirrored to the original location with the original velocity reversed (Figure 4.1).

4.3.3 Pressure

Since density and pressure are related by an overlying equation of state, to simulate a pressure difference the boundary nodes perpendicular to the pressure gradient are set to a constant density. These are fixed after every collision step as described by Pan et al. [72]. An alternative to this boundary condition is to include the pressure gradient as a force term in each fluid.

4.4 Concluding remarks

There is an extensive body of work that proves the validity of SC simulations for natural systems [23, 39, 72, 77] by comparing them to laboratory experiments. Ju [42] showed that the LBM provides consistent results with laboratory experiments of a fluid velocity field in a rough fracture.

Chapter 5: Numerical benchmarks

In this chapter, the development of the multiphase model is presented step-by-step following the concepts defined in Chapter 2. Also, the appropriate validations are presented at each stage of the process.

5.1 Flow through a pair of smooth parallel surfaces

To assess the accuracy of the LBM for our problem of interest, we performed a simulation of a fluid flowing through a pair of parallel infinite plates. The script was written in MATLAB (the code can be found in Section 8.1) and can be run on a personal computer. This was written following the guidelines published by Sukop and Thorne [91]. In the domain, the solid boundaries are set using a bounce back condition (x-direction), and a periodic boundary is selected to simulate an infinite channel in the y-direction. The comparison of the numerical result with the analytical solution of flow through a slit is presented in Figure 5.1. The LBM result converges with the analytical solution after 2 000 iterations.

5.2 Interfacial tension

For carrying out the multiphase flow simulations, the open source LBM code Palabos (`www.palabos.org`) was used. The simulations were run in Stampede2 supercomputer clusters (`www.tacc.utexas.edu/systems/stampede2`).

In the multiphase Shan-Chen model, the parameter G_c (Equation 4.7) controls the interaction force between the two phases, so the interfacial tension is not explicitly set. To calculate the interfacial tension of our system, we carried out a simulation where we placed

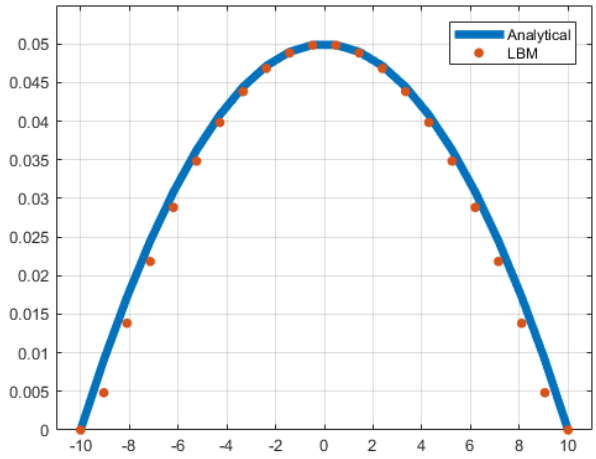

Figure 5.1: Comparison between the analytical solution and the result of our LBM code for a flow through a slit problem. The fracture aperture is 20 lattice units (x-axis).

Table 5.1: Input parameters used for the Shan-Chen model.

Variable	**Description**	**Value**
ρ_1 and ρ_2	Fluid densities	2.00
τ	Relaxation-time	1.00
ρ_d	Dissolved density	0.06
G_c	Cohesion force strenght	0.90
F_1 and F_2	Fluid force	0
ϵ	Convergence threhold	5e-6

a blob of a fluid (we called it fluid 1) in a cube filled with another fluid (fluid 2). The input parameters are described in Table 5.1, and diagram of the initial conditions is shown in Figure 5.2a. For numerical stability, we chose the relaxation time to be equal to one; hence the density and the viscosity of both fluids are equal (studies show that high viscosity ratios lead to numerical instabilities [14]). We set all the boundaries to be periodic.

Since the pressure behavior in the multiphase model is no longer ideal (compared to the single phase model), we used the following equation of state [86, 87] to calculate the pressure field:

$$p = c_s^2(\rho_\sigma + \rho_{\overline{\sigma}}) + c_s^2 G_c \rho_\sigma \rho_{\overline{\sigma}}. \tag{5.1}$$

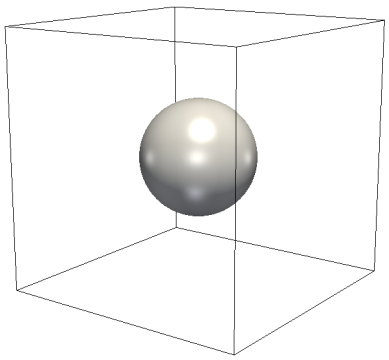

(a) Initial condition

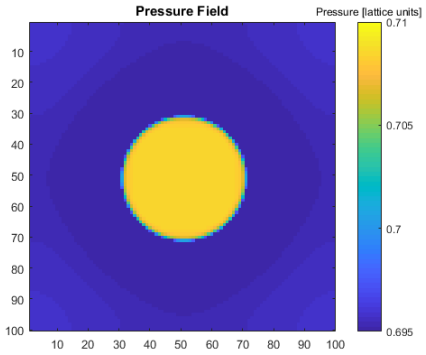

(b) Pressure field

Figure 5.2: Interfacial tension calculation set-up.

Consequently, the pressure at every point can be obtained as:

$$p(x) = \frac{\rho_1(x) + \rho_2(x)}{3}, \tag{5.2}$$

considering that the second term of Equation 5.1 is at least two orders of magnitude smaller than the first one in our numerical set up. The simulation converged after 40 000 iterations from its initial condition, by complying with the following criterion:

$$Energy_{fluid1} \;\&\; Energy_{fluid2} < \epsilon, \tag{5.3}$$

this criterion states that the sum of the momenta of a fluid in every node ($Energy_{fluid}$), has to be less than ϵ for both fluids. The convergence was set to 1e-5. A detailed study on this parameter is presented in Section 5.4.1. Then the interfacial tension was calculated using Equation 2.2. A slice of the pressure field is shown in Figure 5.2b. The interfacial tension of the system resulted in 0.15 [lattice units], consistent with other studies (Figure 5.3).

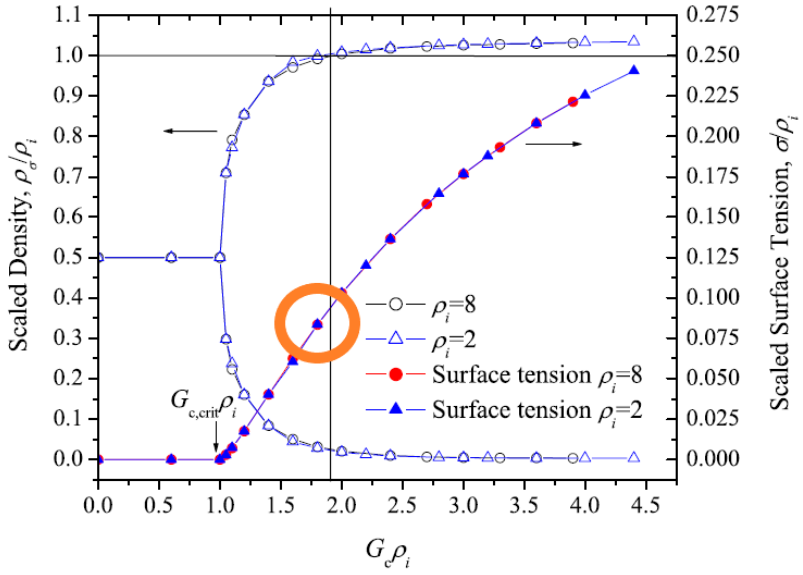

Figure 5.3: Interfacial tension results by Huang et al. [34], where our case (burnt orange circle) matches their numerical results.

5.3 Contact angle

To simulate a pair of wetting and non-wetting fluids, we used the model proposed by Huang et al. [35]. For this, a relationship between the macroscopic contact angle with the fluid-fluid and fluid-solid interaction parameters is suggested as follows:

$$cos\theta_\sigma = \frac{G_{ads,\overline{\sigma}} - G_{ads,\sigma}}{G_c \frac{\rho_\sigma - \rho_{d,\overline{\sigma}}}{2}}. \tag{5.4}$$

The static contact angle between a droplet and a wetting/non-wetting surface was compared with Young's equation. The result of the 3D simulation is pictured in Figure 5.4. Table 5.2 shows the contact angle measurement done with a 2D slice of the domain (the code used to measure the contact angle is included in Section 8.3).

Table 5.2: Comparison of the contact angles results of our model (for the wetting and non-wetting cases) with the analytical equation.

$G_{ads,1}$	Equation 5.4 [°]	3D Simulation [°]
0.4	156.4	154.02
-0.4	23.6	24.1

Figure 5.4: 3D results of the contact angle simulations (156.4^o and 23.6^o respectively).

5.3.1 Advancing and receding angles

We tested the ability of the model to simulate advancing and receding contact angles (contact angle hysteresis), with a domain comprised by 3 capillary tubes with different fluid-solid interaction parameters (neutral, non-wetting, and wetting). Figure 5.5 shows a snapshot of 3 blobs a fluid being displaced by a pressure gradient along a tube. For the neutral and the wetting case there is a significant difference on the advancing and receding contact angle due to the deposit of films [92].

5.4 Capillary tubes

To validate the physics of immiscible displacement in capillary controlled regimes, we carried out a capillary tube intrusion test. This was done by using a bundle of parallel tubes with decreasing diameters as our domain, and setting pressure boundary conditions at the two ends of the tubes as shown by Figure 5.6. Since the pressure increments are very small, the invading fluid velocity was kept very slow, maintaining the capillary number under 10^{-6}.

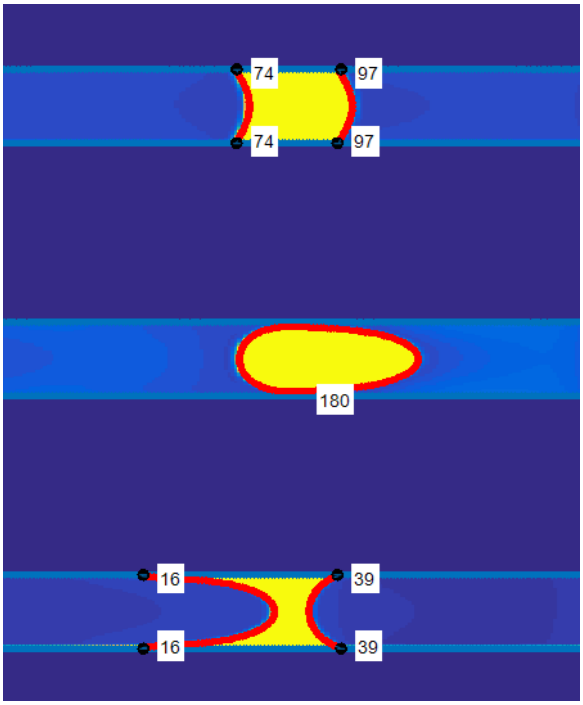

Figure 5.5: Advancing and receding contact angles for an unsteady simulation of blobs being displayed through three tubes exhibiting contact angles of 90^o, 156.4^o, and 23.6^o from top to bottom. The white boxes show the computed contact angles from a 2D slice of the 3D domain computed with the code in Appendix 8.3.

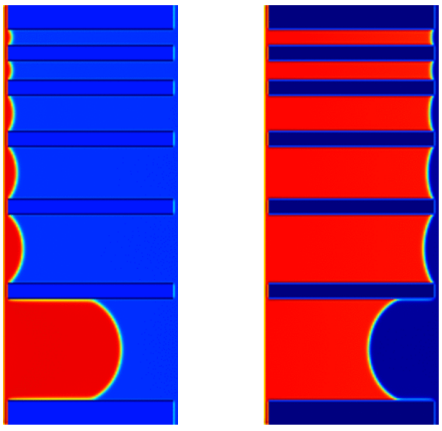

Figure 5.6: Simulation domain exhibiting capillary tubes of decreasing radius. From bottom to top, the radius of the tubes are 30, 20, 15, 10, 6, and 4 lattice units respectively. The picture on the left shows the intrusion of the first drainage step, to the right; the last imbibing front is taking place.

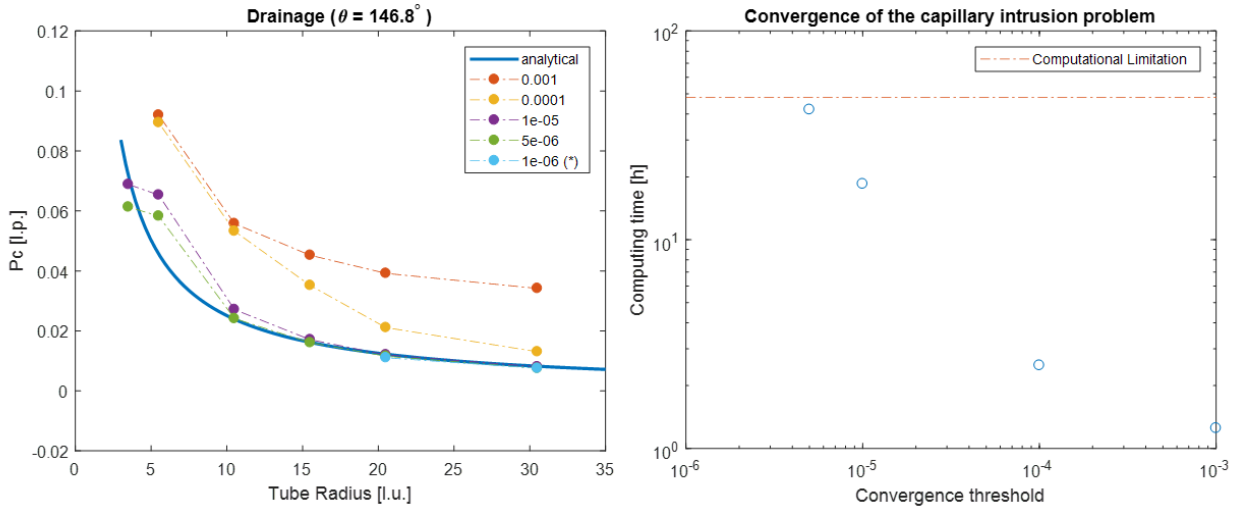

Figure 5.7: Drainage simulation results for different convergence thresholds (ϵ from Equation 5.3) with their respective computing times. In the plot to the left, the capillary pressure to drain each of the tubes from Figure 5.6 is shown, compared to the analytical solution from Washbrun's equation (in solid blue). Although the precision increases with smaller convergence thresholds, the computing time (right plot) increases until reaching the maximum allowed computing time of Stampede2 (48 hrs).
(*) exceeded the supercomputer's maximum computing time allowed (48 hrs).

5.4.1 Computational efficiency test

To test the most efficient convergence parameter (ϵ from Equation 5.3) that provided accurate results in a timely manner, we conducted a series of simulations using the capillary tubes domain, using different orders of magnitude for ϵ. The results of the experiment, and the comparison with the analytical solution are shown in Figure 5.7.

Selecting the ϵ that provided the most accurate results, an imbibition processes was simulated on the same domain. The numerical and analytical solution comparison can be found in Figure 5.8.

5.4.2 Concluding remarks

As shown in this section, the multiphase Shan Chen model of the Lattice Boltzmann method is able to accurately describe the capillary effects of a binary fluid system.

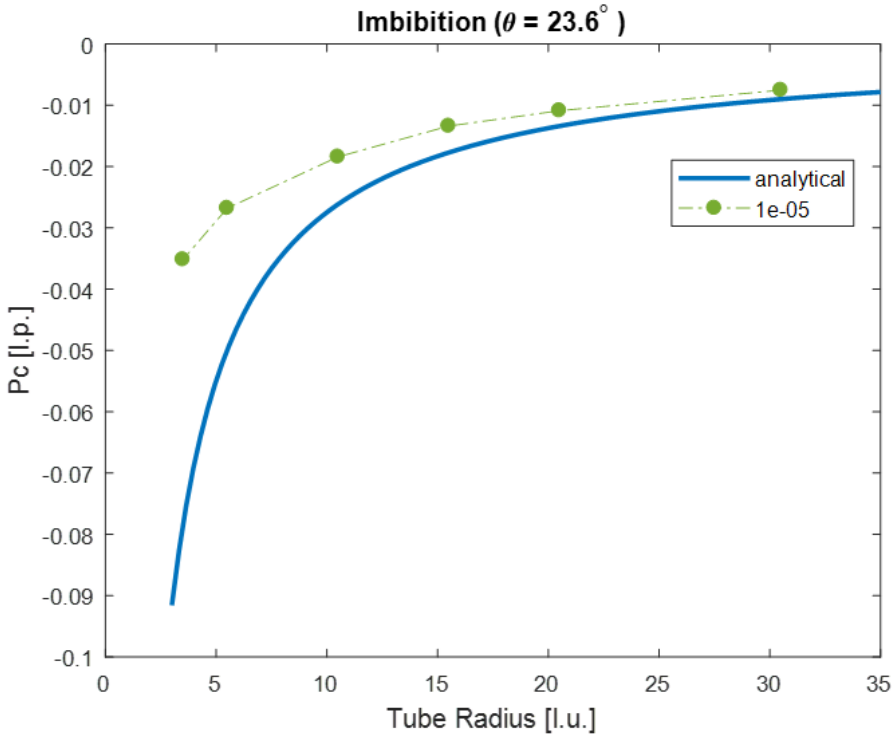

Figure 5.8: Imbibition simulation results using $\epsilon = 5e - 6$ (the most accurate threshold from the drainage experiment shown by Figure 5.7). The results are not as accurate as the drainage simulation due to the limitations of the LBM to capture all the mechanisms of the imbibition process.

Chapter 6: Case studies

In this section we present the results, and an analysis of the numerical experiments we carried out to test the effect of surface heterogeneities on invasive fronts for different domains.

6.1 Heterogeneous wettability

The next two cases present simulations that were carried out to assess the effect of heterogeneous mineralogy (given that each mineral is represented by a different contact angle) in flat surfaces. For convenience, we defined a non-wetting contact angle of 23.6^o and a non-wetting one of 156.4^o throughout this section.

Studies have shown that minerals affect fluid patterns, causing deviations from ideal displacements [17]. Each of the minerals present in a rock surface has a distinct affinity for the fluids in contact with it [16]. Below we present two cases that exhibit simple patterns of surface heterogeneities and an analysis of the flow results.

6.1.1 Striped patterned heterogeneous wet flat surfaces

To evaluate the impact of a heterogeneously-composed surface, a pair of smooth parallel plates was used as a domain, and a pattern of alternating wetting and non-wetting stripes was created on the surface contacting the fluids as shown by Figure 6.1.

To assess the effect of these heterogeneities, a displacing fluid (red) was injected through a plane perpendicular to the x-axis. Both ends of the x-axis were given pressure boundary conditions. The pressure of the boundary at x=0 was increased in small steps (assuring capillary number $< 10^{-6}$) until the initial fluid reached irreducible saturation

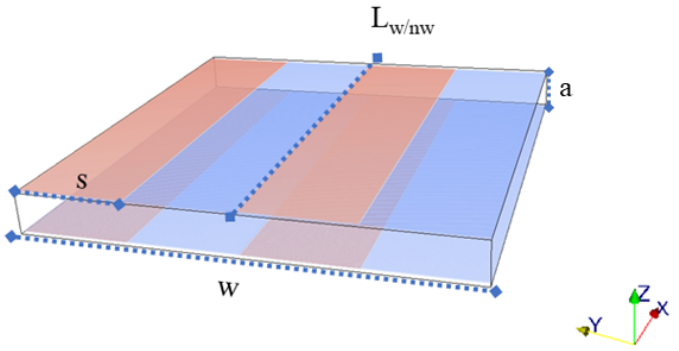

Figure 6.1: Striped wettability surface pattern. The red striped wets (156.4^o) the invading fluid, while the blue stripes are non-wetting (23.6^o). $L_{w/nw}$ stands for the length of the intersection between the wetting and non-wetting patches in the solid phase, w for the width of the fracture, s for the strip width, and a for the aperture.

(complete drainage). The y-axis was given periodic (infinite) boundary conditions.

6.1.1.1 Efficiency test

The code (Palabos) is parallelized with CPUs using MPI [26]. Recent studies suggest that implementing the algorithm in general-purpose graphics processing units (GPGPUs) could yield in an order of magnitude faster solutions [8]. Such implementation is beyond the scope of this thesis.

To test the ideal number of computing nodes to use, we ran a sensitivity analysis using the Stampede2 supercomputer, with the previously calculated ϵ. From Figure 6.2 is visible that the running time plateaus after adding more than 10 nodes (Stampede2 has 68 processors per node), improving only slightly when using 100.

6.1.1.2 Results

The aperture (a) and the number of stripes were varied to assess their relative importance. For convenience the variable $L_{w/nw}$ was introduced, which stands for the length of the intersection between the wetting, and non-wetting patches in the solid phase (Figure 6.1).

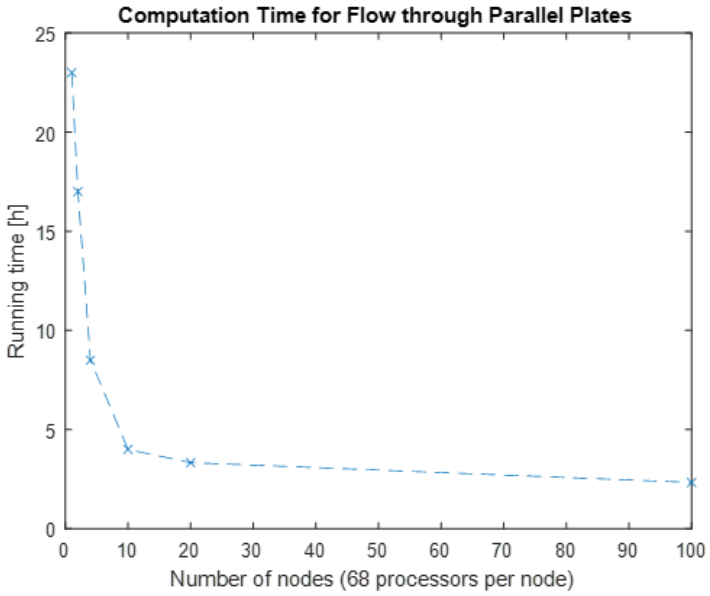

Figure 6.2: Computation time to achieve convergence for multiphase flow through parallel heterogeneous wet plate problem.

Since there is a smooth gradient present in the density distribution functions, the fluid interface was defined with a density threshold $\rho_t = \frac{\rho_1+\rho_2}{2}$, to locate its position. As shown by Pan [73], discretization effects in the interface are visible depending on the domain size.

To normalize the capillary pressure corresponding to different apertures, we introduce a *critical pressure* term, which corresponds to the pressure needed to completely drain wetting fluid from a fracture with homogeneous surface mineralogy using a non-wetting fluid (from Equation 2.3):

$$P_{c_{crit}} = \frac{2\sigma}{a} cos(156.4). \tag{6.1}$$

The length of the interface was measured from a 2D cross section made through the middle of the domain in z-direction to get an estimation of the number of fingers that were formed.

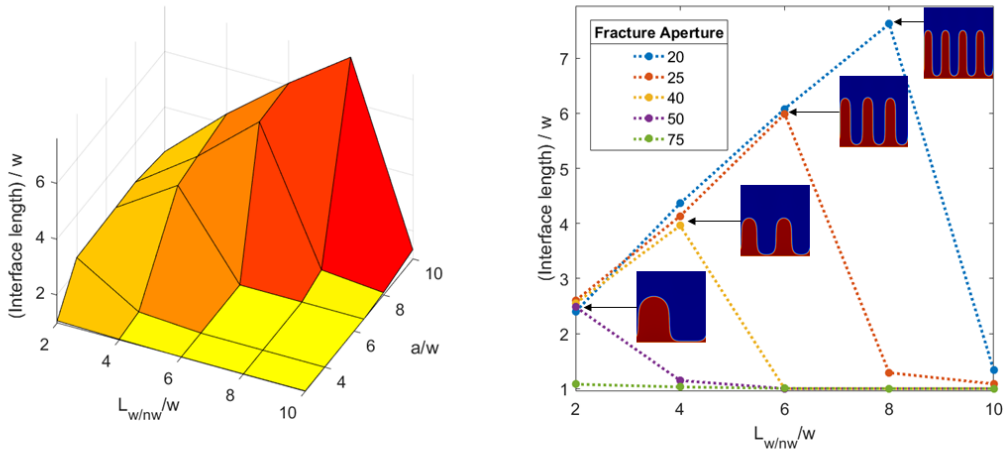

Figure 6.3: Normalized interfacial length (front length/domain length) for 25 cases exhibiting difference in aperture and number of stripes.

6.1.1.3 Discussion

Some of our experiments exhibited capillary fingering (Figure 6.5) that affected the pressure saturation curves. As demonstrated in published work [71], the presence of fingers in EOR processes significantly decrease their efficiency. From Figure 2.6, our simulations fall in the stable capillary fingering region (log(Ca)<-6 and log(M)=0). Although this phenomenon was observed in low aperture areas, whenever the aperture was increased sufficiently these effects were not as pronounced, like Figure 6.5 suggests. From Figure 6.5, it is clear that there is a parameter that controls the formation of capillary fingers in the domain (we denote it with G). The analysis shows that a ratio of the fracture aperture with the width of the strip acts as a threshold for the creation of this instabilities (longer interfacial length).

With the formation of fingers, the capillary-pressure curves increase up to 250%

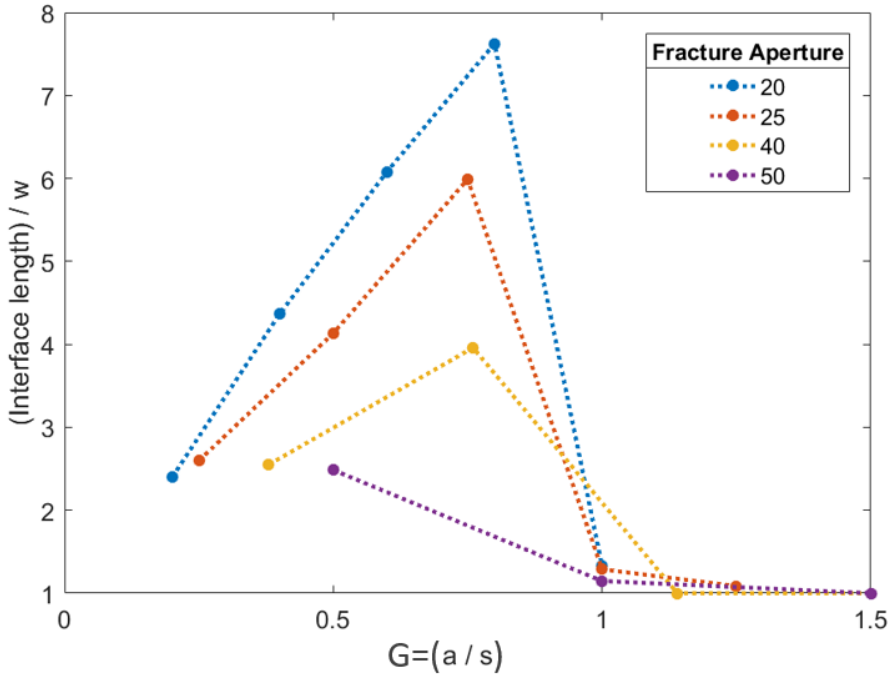

Figure 6.4: Normalized interfacial length vs the ratio of aperture over the length of the stripe. There is a critical geometric factor (aperture/(feature length)), that when approaches unity, flow instabilities (capillary fingering) no longer occur.

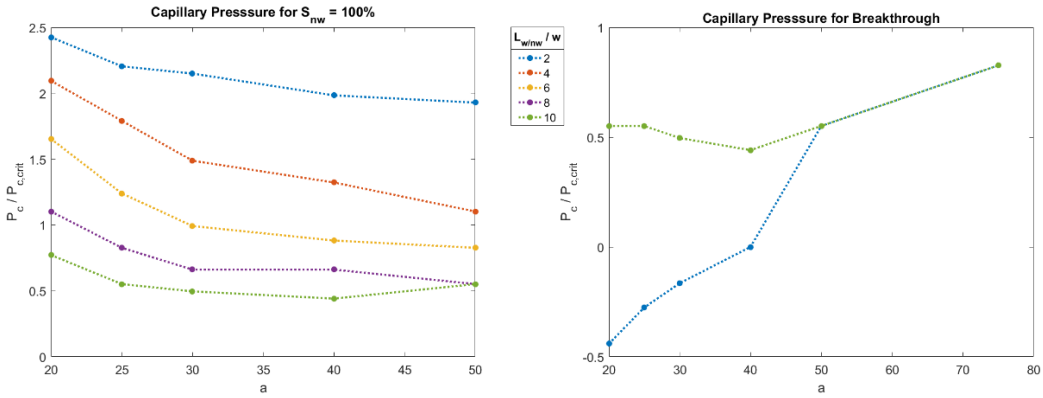

Figure 6.5: Normalized capillary pressure curves for complete drainage (left) and breakthrough (right). Cases with an increasing number of stripes are presented with different colors. The capillary pressure was normalized using Pc_{crit}, which corresponds to the pressure to drain a completely non-wetting fracture with no stripes. Fingering has an adverse effect on the full drainage curve, exhibiting pressures up to 2.5 times the critical capillary pressure. In the smallest aperture domains, spontaneous imbibition was seen at breakthrough.

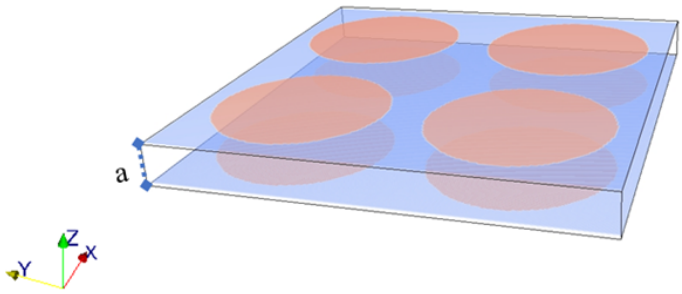

Figure 6.6: Simulation domain exhibiting non-wetting disks.

(Figure 6.5) from the predictions of the analytical model.

6.1.2 Round heterogeneous wet features on flat surfaces

Similarly to the experiments conducted in the domains mentioned above, we ran immiscible displacement simulations through a domain comprised by a wetting surface with non-wetting disks placed on top as pictured in Figure 6.6. The critical geometric values for the two domains simulated are presented in Table 6.1.

Table 6.1: Critical geometric ratio of the simulations exhibiting non-wetting disks (Figure 6.7).

Case	Color	G
1	Blue curve	0.5
2	Red curve	1.25

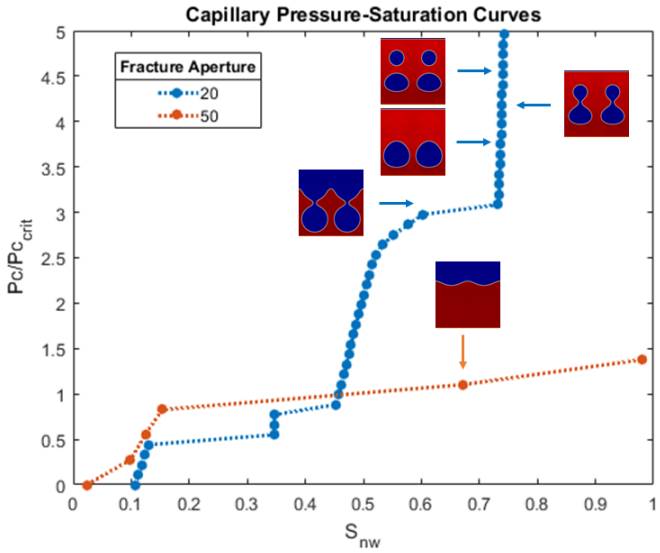

Figure 6.7: Capillary pressure-saturation curves for the two cases of non-wetting disks. The pictures show cross sections of the flow simulation, where the blue fluid is being displaced by the red one.

6.1.3 Discussion

Similarly to the striped domain, the domain with disks was more affected by the wettability of the solid surfaces when they had geometric factors (G) below 1. As seen in the cross sections of the displacement simulation on Figure 6.6, there was contact angle pinning [43] that impeded the fracture to drain completely.

The heterogeneities of flow (in the case, capillary fingering and contact line pinning) observed in the simulations, make this problems unsuitable to be solved by a continuum approach [6], because the REV concept is not satisfied.

6.2 Rough surfaces

In natural rock fractures, the geometries are much more complex due to the processes that generate them. In these domains, the aperture distributions are highly heterogeneous and they have contact points which support the void space, creating additional difficulties for flow. All these makes the configuration of the fluid phases more complex than in the idealized geometries studied before [79].

To study the effect of geometry heterogeneity in fractures, we created synthetic domains. There are three main methods to construct self-affine fracture walls: the Fourier transformation [74], the randomization of the Weierstrass function [62], and the successive addition method [23]. For this work, a fast Fourier transform approach was used to generate a pair of self-affine rough surfaces. In this particular problem, we are assuming that the fracture surfaces are impermeable. Other studies have investigated the effect of fracture-matrix interaction [78].

A pair of rough surfaces was built using *Synfrac*, the input parameters (Figure **??**) that were utilized to recreate the fractures were originally obtained by measuring an induced fracture in a sandstone core with a profilometer.

For this study, the fractal dimension was the variable to study the effect of surface roughness. We selected a range starting from 2.5 to 2.9, to obtain increasingly rougher surfaces which have been measured in different natural settings [45]. We first conducted a spatial continuity analysis to calculate the geometric factor (G) which was done using the experimental variogram [81].

First we selected an appropriate subsection of our original domain (512x512), that complied with being stationary (defined as a size where we observe spatial invariance of the statistic of interest around the domain). The processes of selection, and the verdict of stationarity is shown in Figure 6.8. Calculating the experimental variogram is a computationally intensive process, having a stationary subset of the original domain helps to speed

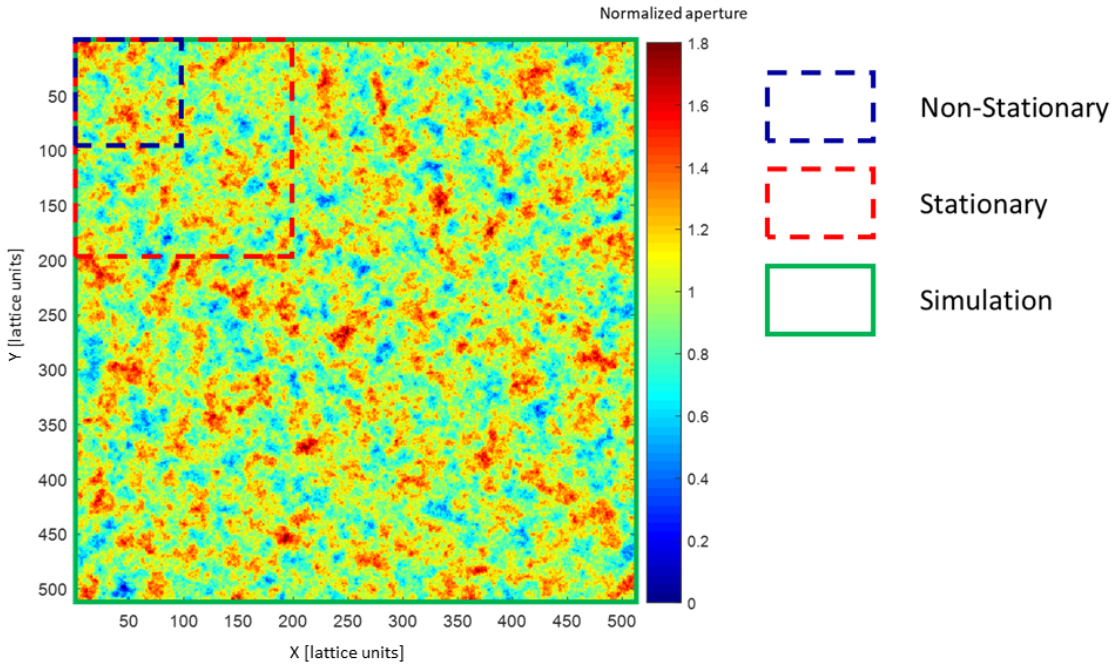

Figure 6.8: Fracture aperture field, the scale is normalized with the average aperture. Red shows the wider apertures, in dark blue are the contact points. The dashed squares depict selections for stationarity test. The first square (blue) represents a domain size of 100x100, the next in size 200x200, following by the entire domain (512x512). The two later ones prove stationary.

up the calculations.

For this experiment, we used 5 synthetic fractures with different fractal exponents. The aperture fields of the fractures are shown in Figure 6.9.

To calculate the size of the surface heterogeneities, an isotropic experimental variogram was calculated on the 5 fracture domains. The plots can be seen in Figure 6.10. The variogram describes the degree of spatial self-dissimilarity; measuring the correlation length of a certain property. In the plot is visible that with an increase of fractal dimension (hence roughness) the variogram yields in a higher nugget effect (short scale discontinuity), due to the local roughness (the amplitude of the short wavelength is decreased), this nugget effect goes from 20 to almost 50 % for the roughest surface. Another observation that can be extracted from the variogram is that the range of spatial correlation of the aperture field decreases with the fractal exponent (G gets smaller).

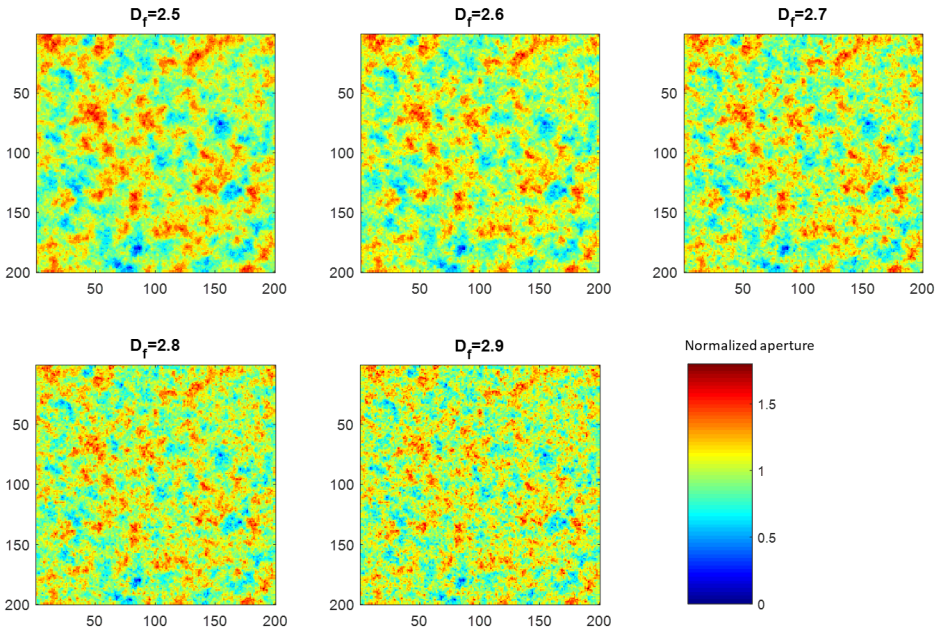

Figure 6.9: Fracture aperture fields with different surface roughness. The fractal exponent (shown in bold) is used to defined the amplitude of the Fourier components.

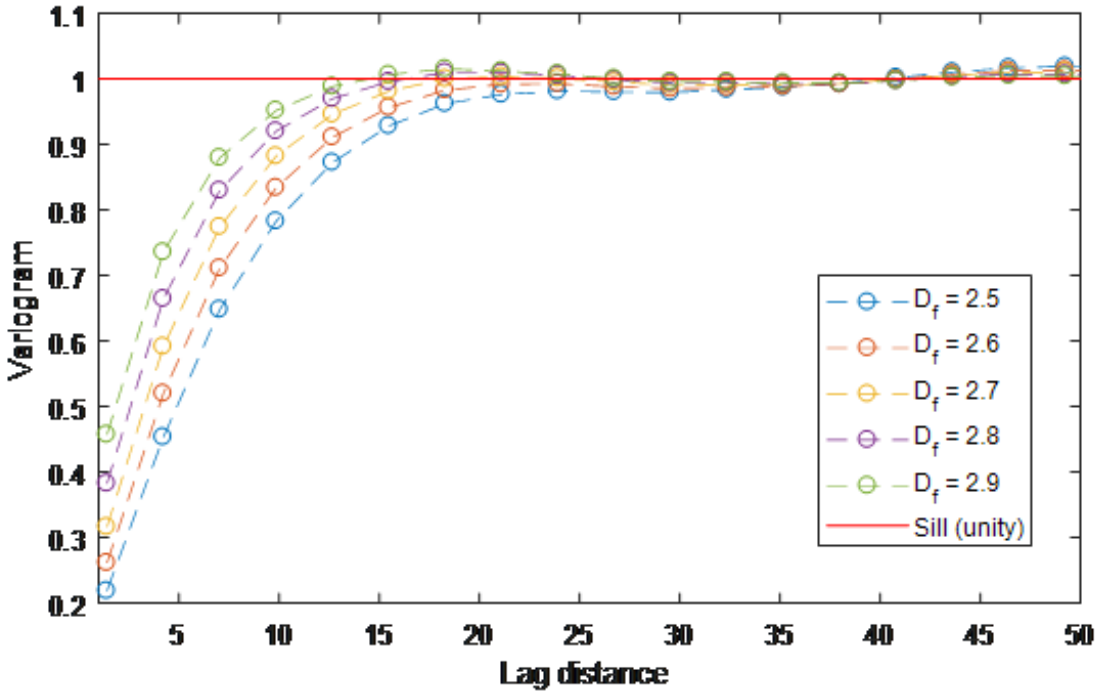

Figure 6.10: Aperture field isotropic variogram of the of the 5 fractures.

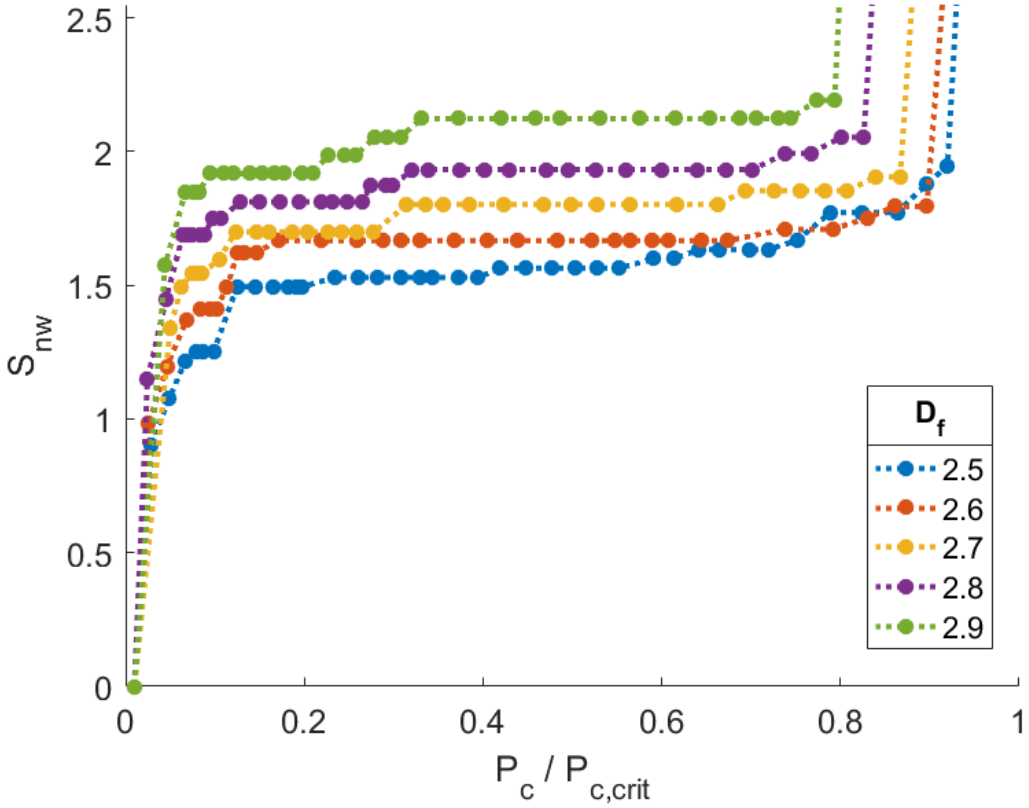

Figure 6.11: Capillary pressure-saturation curve for drainage of the different domains. The critical pressure (Equation 6.1) was calculated with the average fracture aperture.

6.2.1 Results

As expected, the capillary pressure curves become steeper with an increase of the roughness exponent Figure 6.11, due to the increased complexity of the flow paths. Also, the residual water saturation increases in higher fractal exponent surfaces.

6.2.2 Discussion

We found that the standard distribution of fracture apertures (measured on a point-by-point basis), controls the residual saturation of the initial fluid. When the standard deviation of the aperture is larger, there are more crevasses for the fluid to be trapped,

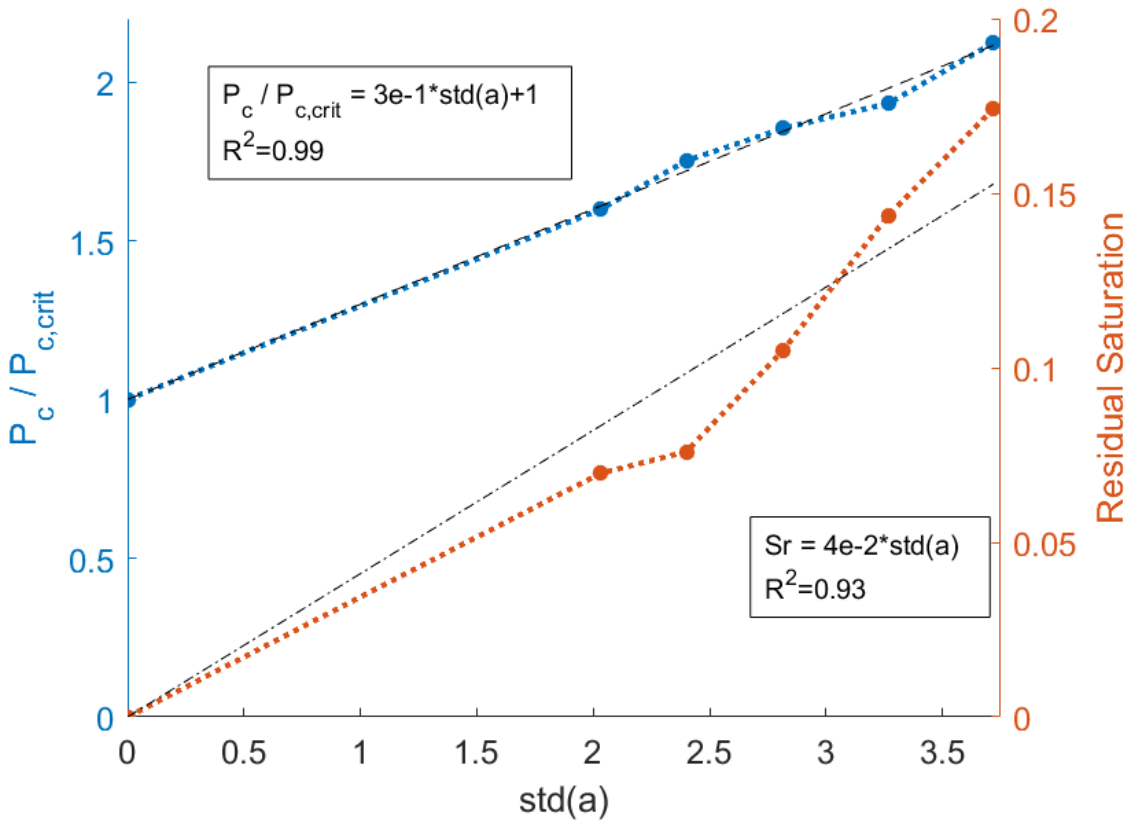

Figure 6.12: Normalized capillary pressure (left axis) and residual saturation (right axis) plot against standard deviation in aperture. The proposed models are shown in black dotted lines.

although, in smoother surfaces the blobs of trapped fluid are bigger (as shown in Figure 6.13). This observations are consistent with laboratory experiments [66], and mathematical proofs [104]. Consequently, with wider standard deviation of the aperture, higher capillary pressure was necessary to percolate the domain (Figure 6.12). In conclusion, the rougher fractures maintained a more homogeneous front due to there big geometric factor (Table 6.2), so the surface heterogeneities disturbed the flow on a lesser manner.

6.3 Heterogeneously-wet rough surfaces

Utilizing multipoint statistics [90], a mineralogy map was produced (Figure 6.14, left) based on a segmented SEM image used as a training input. The most relevant feature

Table 6.2: Critical geometric ratio of the fracture domains, this coefficient is calculated $G = a/\frac{1}{2}range$

Fractal Dimension (D_f)	Geometric Ratio (G)
2.5	0.47
2.6	0.73
2.7	1.48
2.8	1.93
2.9	2.66

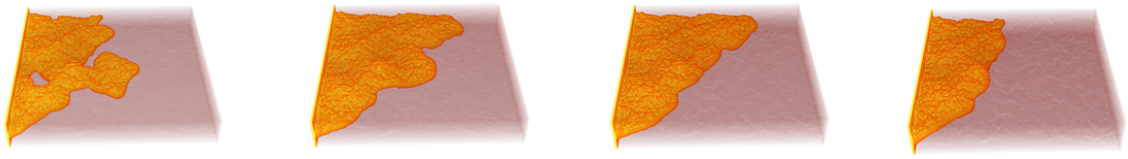

Figure 6.13: Fracture aperture fields with different surface roughness. The fractal exponent (shown in bold) is used to defined the amplitude of the Fourier component.

of the image, is that there is a phase connected across the domain (b) and an isolated one (a).

It has been shown, that these images are appropriate to represent multiscale sources of information on a single domain [29]. To study the importance of connected structures, we carried out imbibition simulations in the roughest of our fractures (D_f=2.9, where the advance of the front was the most homogeneous) mapping the wettability of the system with our stochastic realization.

6.3.1 Discussion

Simulations show that the connectivity of the wetting phase plays a critical role in fluid breakthrough. Even though the paths are more tortuous in Figure 6.14 (panel 2), the imbibition front breaks through at the same time. Also, the fluid trapped in the corners (blue speckles on the red fluid), remain the same.

In the first case, the fluid is not able to overcome the area where the geometric factors of the aperture and non-wetting surface were less than 1. Another observation is

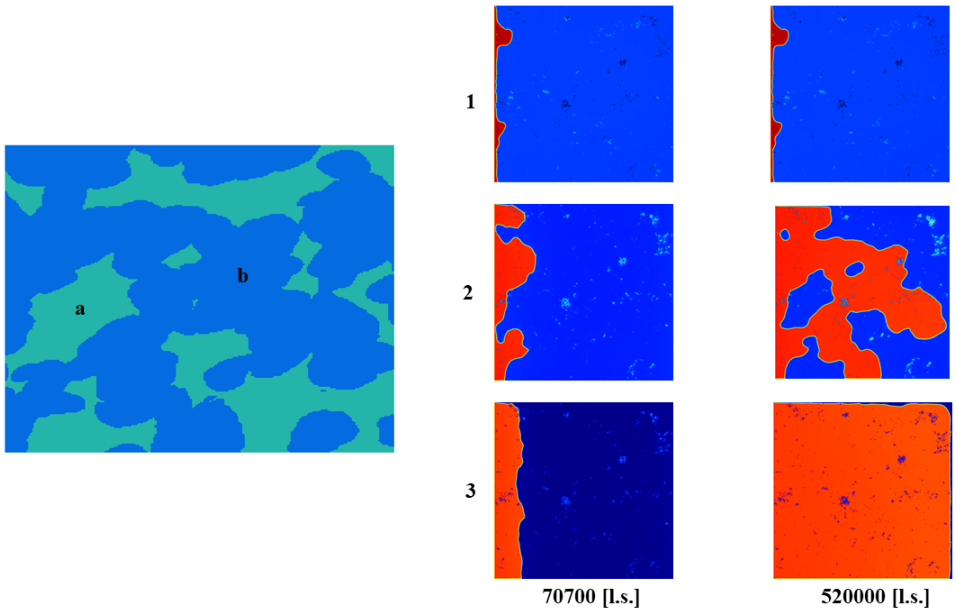

Figure 6.14: Imbibition tests at different times for 3 different rough domains. On the left, the mineralogy map is shown, where a (green) and b (blue) refer to different mineralogy. On the right, three different cases are exemplified: 1) Patch a is wetting, b is non-wetting, 2) Patch a is non-wetting, b is wetting, 3) The entire surface is wetting. The images show a domain cross section, where on the invasive fluid is sown in red.

that typically, it is assumed that the non-wetting phase would not be trapped. Nevertheless, under heterogeneous wetting conditions the simulation results show that this can happen, due to the non-uniform aperture distribution.

These simulations give insight on how the concept of relative permeability through fractures is non-trivial. While this is done in a single fracture, in flow through fracture networks we anticipate that these effects will propagate and the deviations from ideal solutions would be bigger.

Chapter 7: Conclusion

Direct simulations of drainage and imbibition were performed on digitally constructed domains to assess the effect of surface heterogeneity in flow through fractures. The influence of roughness (quantified by fractal dimension), and mineralogy was studied individually to evaluate the most relevant variables that affected multiphase flow displacements. It was found that the ratio of aperture over the heterogeneity size (G) controls the formation of features such as fingers, contact line pinning and channeling; and causes steeper capillary pressure curves. It has been demonstrated that there is a threshold that characterizes the change in behavior.

To account for the size of the aperture clusters, the isotropic variogram was used. It is shown that higher fractal dimensions results in shorter spatial continuity. The domains exhibiting high spatial continuity displayed heterogeneous fronts due to the low geometrical ratio (less than 1). On the other hand, there is linear correlation of the standard deviation of apertures with trapped fluid fraction and capillary pressure increase. Clusters of trapped fluid are bigger for smoother surface (if they exist), but the residual saturation in the overall domain is higher for the rougher domains.

7.1 Future work

The Shan-Chen model of the lattice-Boltzmann method is a powerful method to simulate multiphase flows in realistic geometries. Setting it up, testing it, and validating it were the most time-consuming tasks of the present work. However, after this is done, it could be used to test different cases.[1]

There are open questions left by this work that future research could address. For

[1] All of the code used in this work is available upon request

instance, expanding Lenormand's diagram to account for heterogeneous wettability and surface roughness, to get a clearer picture of when and how this affects different flow regimes.

Another unresolved question is how fluid flow is affected by confining pressures. This can be investigated by coupling the flow with a geomechanical model to understand how changes in aperture distribution affect capillary displacements. Further, reactive transport simulation (dissolution, for instance) could be a fruitful research area for lattice-Boltzmann methods.

For unconventionals, a study of propped fractures and permeable fracture surfaces with variable wettabilities could enhance the current understanding of production mechanisms, and how different scales interact.

Finally, to improve the present code, and to able to simulate smaller domains (Knudsen flows) the implementation of an multi-relaxation time scheme [18] could be a useful addition. A multiscale domain simulation by using advance statistical techniques (machine-learning) could be used to calculate reservoir scale parameters and interactions between different scales.

Chapter 8: Appendix

In this appendix, the MATLAB scripts that were developed during my master's degree are presented.

8.1 MATLAB code for single phase flow through a slit

```
%LBM Simulation of Flow Through a slit
%Javier E. Santos
%Special thanks to Rui Xui for the LBM insights



%data
t_final=10000; %[ts]
n=9; %number of discrete velocities
lx=5; %fracture aperture [lu]
tau=1; %relaxation time (1 is the best for numerical convergence)
nu=(1/3)*(tau-1/2); %Dinamyc viscosity [lu2/ts]
re_no=4.4; %Reynolds number [u_avg*2a/nu]

%slit flow
u_max=0.05; %Max velocity allowed [lu/ts]
u_avg=(2/3)*u_max; %Avergae velocity thtough the slit
ap=((re_no*nu/u_avg)/2)-1; %Aperture of the slit [lu]
ly=int8(2*ap+2);
```

```
g=3*u_avg*nu/ap^2; %From u_avg=(2/3)G* a^2/(2mu)

rho_i=1;

is_solid_node=zeros(ly,lx); %Domain
is_solid_node([1 ly],:)=1;  %Solid boundaries

ex=[0 1 0 -1  0 1 -1 -1  1]; %Discrete velocities
ey=[0 0 1  0 -1 1  1 -1 -1];

w1=4.0/9.0 ;  %Rest weight a=0
w2=1.0/9.0 ;  %Weight a=1,2,3,4
w3=1.0/36.0;  %Weight a=5,6,7,8
cs=1/sqrt(3); %Speed of the lattice

f=ones([size(is_solid_node) n])*(rho_i/n); %Distribution function
f_eq=f;

for ts=1:t_final %Main Loop

ts %Prints time step

for j=(0+1):ly
for i=(0+1):lx
u_x(j,i)=0.0;
u_y(j,i)=0.0;
```

```
rho(j,i)=0.0;

if ~is_solid_node(j,i) %Solid node check
for a=(0+1):n
rho(j,i)=rho(j,i)          +f(j,i,a);
u_x(j,i)=u_x(j,i) +ex(a)*f(j,i,a);
u_y(j,i)=u_y(j,i) +ey(a)*f(j,i,a);
end
u_x(j,i)=u_x(j,i)/rho(j,i);
u_y(j,i)=u_y(j,i)/rho(j,i);
end
end
end

f1=3.0; %Equilibrium distribution function
f2=9.0/2.0;
f3=3.0/2.0;

for j=(0+1):ly
for i=(0+1):lx
if ~is_solid_node(j,i)
rt0=w1*rho(j,i);
rt1=w2*rho(j,i);
rt2=w3*rho(j,i);

ueqxij=u_x(j,i)+tau*g/rho_i; %Gravity force
```

```
ueqyij=u_y(j,i);
uxsq=ueqxij*ueqxij;
uysq=ueqyij*ueqyij;

uxuy5= ueqxij+ueqyij;
uxuy6=-ueqxij+ueqyij;
uxuy7=-ueqxij-ueqyij;
uxuy8= ueqxij-ueqyij;

usq=uxsq+uysq;

feq(j,i,0+1)=rt0*(1                                    -usq/cs^2);
feq(j,i,1+1)=rt1*(1+ueqxij/cs^2+uxsq/cs^4              -usq/cs^2);
feq(j,i,2+1)=rt1*(1+ueqyij/cs^2+uysq/cs^4              -usq/cs^2);
feq(j,i,3+1)=rt1*(1-ueqxij/cs^2+uxsq/cs^4              -usq/cs^2);
feq(j,i,4+1)=rt1*(1-ueqyij/cs^2+uysq/cs^4              -usq/cs^2);

feq(j,i,5+1)=rt2*(1+ uxuy5/cs^2+uxuy5*uxuy5/cs^4-usq/cs^2);
feq(j,i,6+1)=rt2*(1+ uxuy6/cs^2+uxuy6*uxuy6/cs^4-usq/cs^2);
feq(j,i,7+1)=rt2*(1+ uxuy7/cs^2+uxuy7*uxuy7/cs^4-usq/cs^2);
feq(j,i,8+1)=rt2*(1+ uxuy8/cs^2+uxuy8*uxuy8/cs^4-usq/cs^2);

end
end
end
```

```
for j=(0+1):ly %Collision and bounceback loop
for i=(0+1):lx
if ~is_solid_node(j,i)
for a=1:n
f(j,i,a)=f(j,i,a)-(f(j,i,a)-feq(j,i,a))/tau;
end
else
temp=f(j,i,1+1);f(j,i,1+1)=f(j,i,3+1);f(j,i,3+1)=temp;
temp=f(j,i,1+2);f(j,i,1+2)=f(j,i,4+1);f(j,i,4+1)=temp;
temp=f(j,i,1+5);f(j,i,1+5)=f(j,i,7+1);f(j,i,7+1)=temp;
temp=f(j,i,1+6);f(j,i,1+6)=f(j,i,8+1);f(j,i,8+1)=temp;
end
end
end


for j=(0+1):ly %Streaming loop
if j>(0+1)
jn=j-1;  %Periodic bcs
else
jn=ly; %-1 for c
end
if j<(ly) %-1 for c
jp=j+1;
```

```
else
jp=1; %0 for c
end
for i=(0+1):lx
if i>(0+1) %if >1 there are obstacles for flow
in=i-1;
else
in=lx;
end
if i<(lx) %-1 for c
ip=i+1;
else
ip=1; %0 for c
end
ftemp(j ,i ,(0+1))=f(j,i,(0+1));
ftemp(j ,ip,(1+1))=f(j,i,(1+1));
ftemp(jp,i ,(2+1))=f(j,i,(2+1));
ftemp(j ,in,(3+1))=f(j,i,(3+1));
ftemp(jn,i ,(4+1))=f(j,i,(4+1));
ftemp(jp,ip,(5+1))=f(j,i,(5+1));
ftemp(jp,in,(6+1))=f(j,i,(6+1));
ftemp(jn,in,(7+1))=f(j,i,(7+1));
ftemp(jn,ip,(8+1))=f(j,i,(8+1));
end
end
f=ftemp;
```

```
end


x=linspace(-ap,ap,ly);
y_an=g/(2*nu)*(ap^2-x.^2);
plot(x,y_an,'LineWidth',5);
hold on;
plot(x,u_x(:,1),'.','MarkerSize',20); grid on;
xlim([-ap-1 ap+1]);
ylim([0 0.055]);
legend('Analytical','LBM');
title('Flow through a Slit')
xlabel('x [lattice units]')
ylabel('velocity [lattice units]')
```

8.2 MATLAB code for opening vti files

```
%Script to decode a .vti file and generate an isosurface
%Javier E. Santos
%Special thanks to Guillaume Flandin for the decoding insight

vti_struct=xml2struct('Density_field.vti'); %read output file
vti_str=base64decode(vti_struct.VTKFile.ImageData.Piece.PointData.DataArr
vti_no=typecast([0 0 vti_str],'double');
vti_size=str2num(vti_struct.VTKFile.ImageData.Attributes.WholeExtent);
vti_x=vti_size(1)+vti_size(2)+1;
vti_y=vti_size(3)+vti_size(4)+1;
vti_z=vti_size(5)+vti_size(6)+1;
vti_matrix=reshape(vti_no(2:end),[vti_x vti_y vti_z]);
[X,Y,Z] = meshgrid(1:vti_x,1:vti_y,1:vti_z);
isosurface_threshold=1;
[face,vertex,col] = MarchingCubes(X,Y,Z,vti_matrix,isosurface_threshold);
```

8.3 MATLAB code for measuring 2D contact angles from an image

```
%Script to calculate contact angles from a .vti (or any) image
%Javier E. Santos

f.f1_vti_struct=xml2struct('rho1.vti'); %Read density f1 output file
f.f2_vti_struct=xml2struct('rho2.vti'); %Read density f2 output file
f.f1_vti_str=base64decode(f.f1_vti_struct.VTKFile.ImageData.Piece...
PointData.DataArray.Text);
f.f2_vti_str=base64decode(f.f2_vti_struct.VTKFile.ImageData.Piece....
PointData.DataArray.Text);
f.f1_vti_no=typecast([0 0 f.f1_vti_str],'double');
f.f2_vti_no=typecast([0 0 f.f2_vti_str],'double');
vti_size=str2num(f.f1_vti_struct.VTKFile.ImageData.Attributes...
WholeExtent);
vti_x=vti_size(1)+vti_size(2)+1;
vti_y=vti_size(3)+vti_size(4)+1;
vti_z=vti_size(5)+vti_size(6)+1;
rhof1=reshape(f.f1_vti_no(2:end),[vti_x vti_y vti_z]); %Density fluid 1
rhof2=reshape(f.f2_vti_no(2:end),[vti_x vti_y vti_z]); %Density fluid 2
clear f %Saves memory

tp_x=[];
tp_y=[];
tp_z=[];

wall_all=[];
```

```
angle_all=[];
angle_w=[];
angle_nw=[];
angle_n=[];

no_points=3; % Number of points for contact angle calculation

%% Operations
for sl=vti_z/2:vti_z/2 %Slices domain through the middle
slice=squeeze(rhof1(:,:,sl));
image(slice*100);hold on;

slice1=slice;
slice1(slice==0 | slice==0.4 | slice==-0.4 | slice==-0.1 | ...
slice==0.1)=nan; %'remove' solid surface

slice2=slice;
slice2(slice==0 | slice==0.4 | slice==-0.4 | slice==-0.1 | ...
slice==0.1)=-100; %all the solid pixels n,nw

[tt1]=contourc(slice1,[1 1]); %Contour the meniscae
if isempty(tt1)==0

[x_f,y_f,z_f]=C2xyz(tt1); %Arranges the results of the contour matrix
clear tt1
```

```
[tt2]=contourc(slice2,[-99 -99]); %Contours the solid
[x_s,y_s,z_s]=C2xyz(tt2);
clear tt2

k=1;
for i=1:numel(x_s)
clear x_tmp;
clear y_tmp;
x_tmp=double(x_s{i});
y_tmp=double(y_s{i});
for j=1:numel(x_tmp)
x_sol(k)=x_tmp(j);
y_sol(k)=y_tmp(j);
k=k+1;
end
end

scatter(x_sol,y_sol,'filled'); hold on;

for mm=1:numel(x_f) %Number of meniscae
xftmp=x_f{mm}; %Works with individual meniscous
yftmp=y_f{mm};
scatter(xftmp,yftmp,'r','filled'); hold on

first_points_x=[xftmp(1),xftmp(end)];
first_points_y=[yftmp(1),yftmp(end)];
```

```
for i=1:numel(x_sol)
p_dist(i)=sqrt((first_points_x(1)-x_sol(i))^2+...
(first_points_y(1)-y_sol(i))^2);
end

ind=find(p_dist==min(p_dist));
ind=ind(1);
triplepoint_x=x_sol(ind);
triplepoint_y=y_sol(ind);

tp_x(end+1)=triplepoint_x;
tp_y(end+1)=triplepoint_y;
tp_z(end+1)=sl;

if (first_points_x(1)~= first_points_x(2) ...
| first_points_y(1)~= first_points_y(2))==1


scatter(triplepoint_x,triplepoint_y,100,'filled','k');hold on;
line([xftmp(1+no_points),xftmp(1)],[yftmp(1+no_points),...
yftmp(1)]); hold on;
line([x_sol(ind+1),x_sol(ind-1)],[y_sol(ind+1),y_sol(ind-1)]);


if slice2(round(triplepoint_y),round(triplepoint_x+1))>0
```

```
if slice2(round(triplepoint_y+1),round(triplepoint_x+1))>...
slice2(round(triplepoint_y-1),round(triplepoint_x+1))
if y_sol(ind+1)>y_sol(ind-1)
vv=[ (y_sol(ind+1)-y_sol(ind-1)),(x_sol(ind+1)-x_sol(ind-1))];
%solid normal
else
vv=[ (y_sol(ind-1)-y_sol(ind+1)),(x_sol(ind+1)-x_sol(ind-1))];
%solid normal
end
else
if y_sol(ind+1)>y_sol(ind-1)
vv=[ (-y_sol(ind+1)+y_sol(ind-1)),(-x_sol(ind+1)+x_sol(ind-1))];
%solid normal
else
vv=[ (-y_sol(ind-1)+y_sol(ind+1)),(-x_sol(ind+1)+x_sol(ind-1))];
%solid normal
end

end
elseif slice2(round(triplepoint_y),round(triplepoint_x-1))>0
%up and down
if slice2(round(triplepoint_y+1),round(triplepoint_x-1))>...
slice2(round(triplepoint_y-1),round(triplepoint_x-1))
if y_sol(ind+1)>y_sol(ind-1) %up and down
vv=[ (y_sol(ind+1)-y_sol(ind-1)),(x_sol(ind+1)-x_sol(ind-1))];
%solid normal
```

```
else
vv=[ (y_sol(ind-1)-y_sol(ind+1)),(x_sol(ind+1)-x_sol(ind-1))];
%solid normal
end
else
if y_sol(ind+1)>y_sol(ind-1)
vv=[ (-y_sol(ind+1)+y_sol(ind-1)),(-x_sol(ind+1)+x_sol(ind-1))];
%solid normal
else
vv=[ (-y_sol(ind-1)+y_sol(ind+1)),(-x_sol(ind+1)+x_sol(ind-1))];
%solid normal
end

end

elseif slice2(round(triplepoint_y+1),round(triplepoint_x))>0

if slice2(round(triplepoint_y+1),round(triplepoint_x+1))>...
slice2(round(triplepoint_y+1),round(triplepoint_x-1))
if x_sol(ind+1)>x_sol(ind-1) %left right
vv=[ (y_sol(ind+1)-y_sol(ind-1)),(x_sol(ind+1)-x_sol(ind-1))];
%solid normal
else
vv=[ (y_sol(ind+1)-y_sol(ind-1)),(x_sol(ind-1)-x_sol(ind+1))];
%solid normal
end
```

```
else
if x_sol(ind+1)>x_sol(ind-1)
vv=[ (-y_sol(ind+1)+y_sol(ind-1)),(-x_sol(ind+1)+x_sol(ind-1))];
%solid normal
else
vv=[ (-y_sol(ind+1)+y_sol(ind-1)),(-x_sol(ind-1)+x_sol(ind+1))];
%solid normal
end

end

elseif slice2(round(triplepoint_y-1),round(triplepoint_x))>0
if slice2(round(triplepoint_y-1),round(triplepoint_x+1))>...
slice2(round(triplepoint_y-1),round(triplepoint_x-1))
if x_sol(ind+1)>x_sol(ind-1) %left right
vv=[ (y_sol(ind+1)-y_sol(ind-1)),(x_sol(ind+1)-x_sol(ind-1))];
%solid normal
else
vv=[ (y_sol(ind+1)-y_sol(ind-1)),(x_sol(ind-1)-x_sol(ind+1))];
%solid normal
end
else
if x_sol(ind+1)>x_sol(ind-1)
vv=[ (-y_sol(ind+1)+y_sol(ind-1)),(-x_sol(ind+1)+x_sol(ind-1))];
%solid normal
else
```

```
vv=[ (-y_sol(ind+1)+y_sol(ind-1)),(-x_sol(ind-1)+x_sol(ind+1))];
%solid normal
end

end

else
disp('Error')
end

uu=[(yftmp(1+no_points)-yftmp(1)),(xftmp(1+no_points)-xftmp(1)) ];
angle1(mm)=acosd(dot(uu,vv)/(norm(uu)*norm(vv)));
angle_all(end+1)=angle1(mm);
wall_all(end+1)=slice(round(triplepoint_y),round(triplepoint_x));


text(triplepoint_x+2,triplepoint_y+5,num2str(round(angle1(mm))),...
'FontSize',14,'BackgroundColor','w');


%%second angle in meniscous

for i=1:numel(x_sol)
p_dist(i)=sqrt((first_points_x(2)-x_sol(i))^2+...
(first_points_y(2)-y_sol(i))^2);
end
```

```
ind=find(p_dist==min(p_dist));
ind=ind(1);
triplepoint_x=x_sol(ind);
triplepoint_y=y_sol(ind);

tp_x(end+1)=triplepoint_x;
tp_y(end+1)=triplepoint_y;
tp_z(end+1)=sl;

scatter(triplepoint_x,triplepoint_y,100,'filled','k');hold on;
line([xftmp(end-no_points),xftmp(end)],...
[yftmp(end-no_points),yftmp(end)]); hold on;
line([x_sol(ind+1),x_sol(ind-1)],[y_sol(ind+1),y_sol(ind-1)]);


if slice2(round(triplepoint_y),round(triplepoint_x+1))>0
if slice2(round(triplepoint_y+1),round(triplepoint_x+1))>...
slice2(round(triplepoint_y-1),round(triplepoint_x+1))
if y_sol(ind+1)>y_sol(ind-1)
vv=[ (y_sol(ind+1)-y_sol(ind-1)),(x_sol(ind+1)-x_sol(ind-1))];
%solid normal
else
vv=[ (y_sol(ind-1)-y_sol(ind+1)),(x_sol(ind+1)-x_sol(ind-1))];
%solid normal
end
else
```

```
if y_sol(ind+1)>y_sol(ind-1)
vv=[ (-y_sol(ind+1)+y_sol(ind-1)),(-x_sol(ind+1)+x_sol(ind-1))];
%solid normal
else
vv=[ (-y_sol(ind-1)+y_sol(ind+1)),(-x_sol(ind+1)+x_sol(ind-1))];
%solid normal
end

end
elseif slice2(round(triplepoint_y),round(triplepoint_x-1))>0
%up and down
if slice2(round(triplepoint_y+1),round(triplepoint_x-1))>slice2(round(tri
if y_sol(ind+1)>y_sol(ind-1) %up and down
vv=[ (y_sol(ind+1)-y_sol(ind-1)),(x_sol(ind+1)-x_sol(ind-1))];
%solid normal
else
vv=[ (y_sol(ind-1)-y_sol(ind+1)),(x_sol(ind+1)-x_sol(ind-1))];
%solid normal
end
else
if y_sol(ind+1)>y_sol(ind-1)
vv=[ (-y_sol(ind+1)+y_sol(ind-1)),(-x_sol(ind+1)+x_sol(ind-1))];
%solid normal
else
vv=[ (-y_sol(ind-1)+y_sol(ind+1)),(-x_sol(ind+1)+x_sol(ind-1))];
%solid normal
```

```
end

end

elseif slice2(round(triplepoint_y+1),round(triplepoint_x))>0

if slice2(round(triplepoint_y+1),round(triplepoint_x+1))>...
slice2(round(triplepoint_y+1),round(triplepoint_x-1))
if x_sol(ind+1)>x_sol(ind-1) %left right
vv=[ (y_sol(ind+1)-y_sol(ind-1)),(x_sol(ind+1)-x_sol(ind-1))];
%solid normal
else
vv=[ (y_sol(ind+1)-y_sol(ind-1)),(x_sol(ind-1)-x_sol(ind+1))];
%solid normal
end
else
if x_sol(ind+1)>x_sol(ind-1)
vv=[ (-y_sol(ind+1)+y_sol(ind-1)),(-x_sol(ind+1)+x_sol(ind-1))];
%solid normal
else
vv=[ (-y_sol(ind+1)+y_sol(ind-1)),(-x_sol(ind-1)+x_sol(ind+1))];
%solid normal
end

end
```

```
elseif slice2(round(triplepoint_y -1),round(triplepoint_x))>0
if slice2(round(triplepoint_y -1),...
round(triplepoint_x+1))>slice2(round(triplepoint_y -1),...
round(triplepoint_x -1))
if x_sol(ind+1)>x_sol(ind-1) %left right
vv=[ (y_sol(ind+1)-y_sol(ind -1)),(x_sol(ind+1)-x_sol(ind -1))];
%solid normal
else
vv=[ (y_sol(ind+1)-y_sol(ind -1)),(x_sol(ind-1)-x_sol(ind+1))];
%solid normal
end
else
if x_sol(ind+1)>x_sol(ind-1)
vv=[ (-y_sol(ind+1)+y_sol(ind -1)),(-x_sol(ind+1)+x_sol(ind -1))];
%solid normal
else
vv=[ (-y_sol(ind+1)+y_sol(ind -1)),(-x_sol(ind-1)+x_sol(ind+1))];
%solid normal
end
end

else
disp('Error')
end

uu=[(yftmp(end-no_points)-yftmp(end)),(xftmp(end-no_points)...
```

```
-xftmp(end)) ];
angle2(mm)=acosd(dot(uu,vv)/(norm(uu)*norm(vv)));
angle_all(end+1)=angle2(mm);
wall_all(end+1)=slice(round(triplepoint_y),round(triplepoint_x));
text(triplepoint_x-3,triplepoint_y+5,num2str(round(angle2(mm))),...
'FontSize',14,'BackgroundColor','w');
clear vv

else
angle1(mm)=180;
angle2(mm)=180;
text(triplepoint_x-3,triplepoint_y+5,num2str(round(angle2(mm))),...
'FontSize',14,'BackgroundColor','w');
end
end
end
end
```

Bibliography

[1] Alexis, D. A., Karpyn, Z. T., Ertekin, T., and Crandall, D. (2015). Fracture permeability and relative permeability of coal and their dependence on stress conditions. *Journal of Unconventional Oil and Gas Resources*, 10:1–10.

[2] Amott, E. (1958). Observations Relating to the Wettability of Porous Rock. *Petroleum Transactions, AIME*, 216:156–162.

[3] Anderson, W. (1986). Wettability Literature Survey- Part 2: Wettability Measurement. *Journal of Petroleum Technology*, 38(11):1246–1262.

[4] Andrew, M., Bijeljic, B., and Blunt, M. J. (2014). Pore-scale contact angle measurements at reservoir conditions using X-ray microtomography. *Advances in Water Resources*, 68:24–31.

[5] Austad, T. and Milter, J. (1997). Spontaneous Imbibition of Water Into Low Permeable Chalk at Different Wettabilities Using Surfactants. In *International Symposium on Oilfield Chemistry*. Society of Petroleum Engineers.

[6] Bear, J. (1972). *Dynamics of fluids in porous media*. American Elsevier.

[7] Bhatnagar, P. L., Gross, E. P., and Krook, M. (1954). A model for collision processes in gases. I. Small amplitude processes in charged and neutral one-component systems. *Physical Review*, 94(3):511–525.

[8] Briggs, S., Karney, B. W., and Sleep, B. E. (2014). Numerical modelling of flow and transport in rough fractures. *Journal of Rock Mechanics and Geotechnical Engineering*, 6:535–545.

[9] Brown, S. R. (1987). Fluid Flow Through Rock Joints: The Effect of Surface Roughness. *Journal of Geophysical Research*, 92(B2):1337–1347.

[10] Brown, S. R. (1995). Simple mathematical model of a rough fracture. *Journal of Geophysical Research: Solid Earth*, 100(B4):5941–5952.

[11] Brown, S. R. and Scholz, C. H. (1985). Broad bandwidth study of the topography of natural rock surfaces. *Journal of Geophysical Research*, 90(B14):12575.

[12] Cassie, A. B. D. (1948). Contact angles. *Discussions of the Faraday Society*, 3:11.

[13] Cheng, J. T., Pyrak-Nolte, L. J., Nolte, D. D., and Giordano, N. J. (2004). Linking pressure and saturation through interfacial areas in porous media. *Geophysical Research Letters*, 31(8):1–4.

[14] Chin, J. and Coveney, P. V. (2002). Lattice Boltzmann study of spinodal decomposition in two dimensions. *Physical Review E - Statistical, Nonlinear, and Soft Matter Physics*, 66(1):1–8.

[15] Darcy, H. (1856). Les fontaines publiques de la ville de Dijon : exposition et application des principes à suivre et des formules à employer dans les questions de distribution d'eau. *Recherche*, page 647.

[16] Deglint, H., DeBuhr, C., Clarkson, C., Krause, K., Aquino, S., Vahedian, A., and Ghanizadeh, A. (2016). Understanding Wettability Heterogeneity at the Micro and Nano Scale in Unconventional Light Oil Reservoirs. *Unconventional Resources Technology Conference (URTeC)*, pages 1–13.

[17] Deglint, H. J., Ghanizadeh, A., Debuhr, C., and Clarkson, C. R. (2017). Comparison of Micro-and Macro-Wettability Measurements for Unconventional Reservoirs: The Devil is in the Detail. *Unconventional Resources Technology Conference*, (July):24–26.

[18] D'Humieres, D., Ginzburg, I., Manfred, K., Pierre, L., and Li-Shi, L. (2002). Multiple-Relaxation-Time Lattice Boltzmann Models in 3D Multiple-relaxation-time lattice Boltzmann. *NASA*, (AUGUST).

[19] Dijk, P. and Berkowitz, B. (1998). Precipitation and dissolution of reactive solutes in fractures. *Water Resources Research*, 34(3):457–470.

[20] Dixit, A., McDougall, S., Sorbie, K., and Buckley, J. (1999). Pore-Scale Modeling of Wettability Effects and Their Influence on Oil Recovery. *SPE Reservoir Evaluation & Engineering*, 2(01):25–36.

[21] Donaldson, E. C. and Alam, W. (2008). *Wettability*, volume 25.

[22] Dou, Z., Zhou, Z., and Sleep, B. (2013). Influence of wettability on interfacial area during immiscible liquid invasion into a 3D self-affine rough fracture: Lattice Boltzmann simulations. *Advances in Water Resources*, 61:1–11.

[23] Dou, Z. and Zhou, Z.-f. (2014). Lattice Boltzmann simulation of solute transport in a single rough fracture. *Water Science and Engineering*, 7(3):277–287.

[24] Dupuis, A. and Yeomans, J. M. (2004). Lattice Boltzmann modelling of droplets on chemically heterogeneous surfaces. *Future Generation Computer Systems*, 20:993–1001.

[25] Eker, E. and Akin, S. (2006). Lattice Boltzmann simulation of fluid flow in synthetic fractures. *Transport in Porous Media*, 65(3):363–384.

[26] Forum, M. P. (1994). MPI: A Message-Passing Interface Standard. Technical report, Knoxville, TN, USA.

[27] Gale, J. F. W., Reed, R. M., and Holder, J. (2007). Natural fractures in the Barnett Shale and their importance for hydraulic fracture treatments. *AAPG Bulletin*, 91(4):603–622.

[28] Ge, S. (1997). A governing equation for fluid flow in rough fractures. *Water Resources Research*.

[29] Gerke, K. M., Karsanina, M. V., and Mallants, D. (2015). Universal stochastic multiscale image fusion: An example application for shale rock. *Scientific Reports*, 5:1–12.

[30] Gneiting, T. and Schlather, M. (2001). Stochastic models which separate fractal dimension and Hurst effect. (1):1–8.

[31] Gouze, P., Noiriel, C., Bruderer, C., Loggia, D., and Leprovost, R. (2003). X-ray tomography characterization of fracture surfaces during dissolution. *Geophysical Research Letters*, 30(5):n/a–n/a.

[32] Harris, P. M. P. M., Weber, L. J. L. J., American Association of Petroleum Geologists., and SEPM (Society for Sedimentary Geology) (2006). *Giant hydrocarbon reservoirs of the world : from rocks to reservoir characterization and modeling*. The American Association of Petroleum Geologists.

[33] Hassanizadeh, S. M. and Gray, W. G. (1993). Thermodynamic basis of capillary pressure in porous media. *Water Resources Research*, 29(10):3389–3405.

[34] Huang, H., Sukop, M., and Lu, X. (2015). *Multiphase Lattice Boltzmann Methods Theory and Application*, volume 1. John Wiley & Sons.

[35] Huang, H., Thorne, D. T., Schaap, M. G., and Sukop, M. C. (2007). Proposed approximation for contact angles in Shan-and-Chen-type multicomponent multiphase lattice Boltzmann models. *Physical Review E - Statistical, Nonlinear, and Soft Matter Physics*, 76(6):1–6.

[36] Iglauer, S., Salamah, A., Sarmadivaleh, M., Liu, K., and Phan, C. (2014). Contamination of silica surfaces: Impact on waterCO2quartz and glass contact angle measurements. *International Journal of Greenhouse Gas Control*, 22:325–328.

[37] Iwahara, D., Shinto, H., Miyahara, M., and Higashitani, K. (2003). Liquid Drops on Homogeneous and Chemically Heterogeneous Surfaces: A Two-Dimensional Lattice Boltzmann Study. *Langmuir*, 19(21):9086–9093.

[38] Jain, V., Bryant, S., and Sharma, M. (2003). Influence of wettability and saturation on liquid - Liquid interfacial area in porous media. *Environmental Science and Technology*, 37(3):584–591.

[39] Jerauld, G. R., Fredrich, J., Lane, N., Sheng, Q., Crouse, B., Freed, D. M., Fager, A., and Xu, R. (2017). Validation of a Workflow for Digitally Measuring Relative Permeability. *SPE Abu Dhabi International Petroleum Exhibition & Conference*.

[40] Jettestuen, E., Helland, J. O., and Prodanović, M. (2013). A level set method for simulating capillary-controlled displacements at the pore scale with nonzero contact angles. *Water Resources Research*, 49(8):4645–4661.

[41] Joanny, J. F. and de Gennes, P. G. (1984). A model for contact angle hysteresis. *The Journal of Chemical Physics*, 81(1):552–562.

[42] Ju, Y., Zhang, Q., Zheng, J., Chang, C., and Xie, H. (2017). Fractal model and Lattice Boltzmann Method for Characterization of Non-Darcy Flow in Rough Fractures. *Scientific Reports*, 7:41380.

[43] Jung, N., Nadkarni, G. D., and Garoff, S. (1992). An Investigation of Microscopic Aspects of Contact Angle Hysteresis: Pinning of the Contact Line on a Single Defect Surfactant effects on droplet dynamics and deposition patterns: a lattice gas model An Investigation of Microscopic Aspects of Contact Angl. *Europhys. Lett*, 20(6):523–528.

[44] Killough, J. (1976). Reservoir Simulation With History-Dependent Saturation Functions. *Society of Petroleum Engineers Journal*, 16(01):37–48.

[45] Krohn, C. E. (1988). Fractal measurements of sandstones, shales, and carbonates. *Journal of Geophysical Research*, 93(B4):3297.

[46] Kusumaatmaja, H., Leopoldes, J., Dupuis, A., and Yeomans, J. M. (2006). Drop dynamics on chemically patterned surfaces.

[47] Kusumaatmaja, H. and Yeomans, J. M. (2007). Modeling contact angle hysteresis on chemically patterned and superhydrophobic surfaces. *Langmuir*, 23(11):6019–6032.

[48] Lake, L., Johns, R., Rossen, W., and Pope, G. (2014). *Fundamentals of enhanced oil recovery*.

[49] Landry, C. J., Karpyn, Z. T., and Ayala, O. (2014). Relative permeability of homogenous-wet andmixed-wet porousmedia as determined by pore-scale lattice Boltzmann modeling. *Water*, 50(5):3672–3689.

[50] Laubach, S. E., O. J. E. and Eichhubl, P, Fomel, S and Marrett, R. A. (2010). Natural Fractures from the Perspective of Diagenesis. *CSEG Recorder*, (SEPTEMBER):26–31.

[51] Lee, H. B., Yeo, I. W., Ji, S. H., and Lee, K. K. (2010). Wettability-dependent DNAPL migration in a rough-walled fracture. *Journal of Contaminant Hydrology*, 113(1-4):44–55.

[52] Lenormand, R. (1990). Liquids in porous media. *Journal of Physics: Condensed Matter*, 2(S):SA79–SA88.

[53] Lenormand, R., Touboul, E., and Zarcone, C. (1988). Numerical models and experiments on immiscible displacements in porous media. *Journal of Fluid Mechanics*, 189(-1):165.

[54] Lenormand, R. and Zarcone, C. (1989). Capillary fingering: Percolation and fractal dimension. *Transport in Porous Media*, 4(6):599–612.

[55] Leslie Zhang, D., Liu, S., Puerto, M., Miller, C. A., and Hirasaki, G. J. (2006). Wettability alteration and spontaneous imbibition in oil-wet carbonate formations. *Journal of Petroleum Science and Engineering*, 52(1-4):213–226.

[56] Li, Q., Zhou, P., and Yan, H. J. (2016). Pinning-Depinning Mechanism of the Contact Line during Evaporation on Chemically Patterned Surfaces: A Lattice Boltzmann Study. *Langmuir*, 32(37):9389–9396.

[57] Mandelbrot, B. B. (1983). *The fractal geometry of nature*, volume 173.

[58] Marrett, R., Laubach, S. E., and Olson, J. E. (2007). Anisotropy and beyond: Geologic perspectives on geophysical prospecting for natural fractures. *The Leading Edge*, 26(9):1106–1111.

[59] Marrett, R., Ortega, O. J., and Kelsey, C. M. (1999). Extent of power-law scaling for natural fractures in rock. *Geology*, 27(9):799.

[60] McNamara, G. R. and Zanetti, G. (1988). Use of the boltzmann equation to simulate lattice-gas automata. *Physical Review Letters*, 61(20):2332–2335.

[61] Méheust, Y. and Schmttbuhl, J. (2001). Geometrical heterogeneities and permeability anisotropy of rough fractures. *Journal of Geophysical Research*, 106:2098–2102.

[62] Milman, V. Y., Stelmashenko, N. A., and Blumenfeld, R. (1994). Fracture surfaces: A critical review of fractal studies and a novel morphological analysis of scanning tunneling microscopy measurements. *Progress in Materials Science*, 38:425–474.

[63] Morrow, N. R. (1970). Physics and Thermodynamics of Capillary Action in Porous Media. *Industrial & Engineering Chemistry*, 62(6):32–56.

[64] Narr, W., Schechter, D. S., and Thompson, L. B. (2006). *Naturally fractured reservoir characterization*. Society of Petroleum Engineers.

[65] Nelson, R. A. (2001). *Geologic analysis of naturally fractured reservoirs*. Gulf Professional Pub.

[66] Neuweiler, I., Sorensen, I., and Kinzelbach, W. (2004). Experimental and theoretical investigations of drainage in horizontal rough-walled fractures with different correlation structures. *Advances in Water Resources*, 27(12):1217–1231.

[67] Ogilvie, S. R., Isakov, E., and Glover, P. W. (2006). Fluid flow through rough fractures in rocks. II: A new matching model for rough rock fractures. *Earth and Planetary Science Letters*, 241(3-4):454–465.

[68] Olson, J. E., Laubach, S. E., and Lander, R. H. (2007). Combining diagenesis and mechanics to quantify fracture aperture distributions and fracture pattern permeability. *Geological Society, London, Special Publications*, 270(1):101–116.

[69] Olsson, W. A. and Brown, S. R. (1993). Hydromechanical response of a fracture undergoing compression and shear. *International Journal of Rock Mechanics and Mining Sciences and*, 30(7):845–851.

[70] Oron, A. P. and Berkowitz, B. (1998). Flow in rock fractures: The local cubic law assumption reexamined. *Water Resources Research*, 34(11):2811–2825.

[71] Orr, F. M. and Taber, J. J. (1984). Use of Carbon Dioxide in Enhanced Oil Recovery. *Science*, 224(4649):563–569.

[72] Pan, C., Hilpert, M., and Miller, C. T. (2004). Lattice-Boltzmann simulation of two-phase flow in porous media. *Water Resources Research*, 40(1):1–14.

[73] Pan, C., Luo, L. S., and Miller, C. T. (2006). An evaluation of lattice Boltzmann schemes for porous medium flow simulation. *Computers and Fluids*, 35(8-9):898–909.

[74] Passoja, D. E. and Amborski, D. J. (1978). Fracture profile analysis by Fourier transform methods. *Microstruct. Sci*, 6:143–148.

[75] Pieters, D. and Graves, R. (1994). Fracture Relative Permeability: Linear or Non-Linear Function of Saturation. In *International Petroleum Conference and Exhibition of Mexico*, Veracruz, Mexico. Society of Petroleum Engineers.

[76] Piri, M. and Karpyn, Z. T. (2007). Prediction of fluid occupancy in fractures using network modeling and x-ray microtomography. II: Results. *Physical Review E - Statistical, Nonlinear, and Soft Matter Physics*, 76(1):1–11.

[77] Porter, M. L., Schaap, M. G., and Wildenschild, D. (2009). Lattice-Boltzmann simulations of the capillary pressure-saturation-interfacial area relationship for porous media. *Advances in Water Resources*, 32(11):1632–1640.

[78] Prodanovic, M. and Bryant, S. (2009). Physics-Driven Interface Modeling for Drainage and Imbibition in Fractures. *SPE Journal*, 14(3):11–14.

[79] Prodanovic, M., Bryant, S. L., and Karpyn, Z. T. (2010). Investigating Matrix / Fracture Transfer via a Level Set Method for Drainage and Imbibition. (March):125–136.

[80] Pruess, K. and Tsang, Y. W. (1990). On two-phase relative permeability and capillary pressure of rough-walled rock fractures. *Water Resources Research*, 26(9):1915–1926.

[81] Pyrcz, M. J. and Deutsch, C. V. (2014). *Geostatistical Reservoir Modeling*. Oxford University Press.

[82] Raeini, A. Q., Blunt, M. J., and Bijeljic, B. (2012). Modelling two-phase flow in porous media at the pore scale using the volume-of-fluid method. *Journal of Computational Physics*, 231(17):5653–5668.

[83] Rasmuson, A. and Neretnieks, I. (1986). Radionuclide Transport in Fast Channels in Crystalline Rock. *Water Resources Research*, 22(8):1247–1256.

[84] Reeves, P. C. and Celia, M. A. (1996). A Functional Relationship Between Capillary Pressure, Saturation, and Interfacial Area as Revealed by a Pore-Scale Network Model. *Water Resources Research*, 32(8):2345–2358.

[85] Romm, E. S. (1966). Flow characteristics of fractured rocks. *Moscow*.

[86] Shan, X. and Chen, H. (1993). Lattice Boltzmann model for simulating flows with multi phases and components. *Physical Review E*, 47(3):1815–1819.

[87] Shan, X. and Chen, H. (1994). Simulation of nonideal gases and liquid-gas phase transitions by the lattice Boltzmann equation. *Physical Review E*, 49(4):2941–2948.

[88] Shibuichi, S., Onda, T., Satoh, N., and Tsujii, K. (1996). Super Water-Repellent Surfaces Resulting from Fractal Structure. *The Journal of Physical Chemistry*, 100(50):19512–19517.

[89] Sinha, P. K. and Wang, C. Y. (2007). Pore-network modeling of liquid water transport in gas diffusion layer of a polymer electrolyte fuel cell. *Electrochimica Acta*, 52(28):7936–7945.

[90] Strebelle, S. (2002). Conditional Simulation of Complex Geological Structures Using Multiple-Point Statistics. *Mathematical Geology*, 34(1):1–21.

[91] Sukop, M. C. and Thorne, D. T. (2007). *Lattice Boltzmann Modeling*. Springer.

[92] Tadmor, R. (2004). Line Energy and the Relation between Advancing, Receding, and Young Contact Angles. *Langmuir*, 20(18):7659–7664.

[93] Tokan-Lawal, A. (2015). *Understanding fluid flow in rough-walled fractures using x-ray microtomography images*. PhD thesis, University of Texas at Austin.

[94] Tokan-Lawal, A., Landry, C. J., Prodanovic, M., and Eichhubl, P. (2014). Understanding Tortuosity and Permeability variations in Naturally Fractured Reservoirs: Niobrara Formation. *Proceedings of the 2nd Unconventional Resources Technology Conference*, pages 1–13.

[95] Tokan-Lawal, A., Prodanovic, M., and Eichhubl, P. (2015). Investigating flow properties of partially cemented fractures in Travis Peak Formation using image-based pore-scale modeling. *Journal of Geophysical Research B: Solid Earth*, 120(8):5453–5466.

[96] Tokan-Lawal, A., Prodanović, M., Landry, C. J., and Eichhubl, P. (2017). Influence of Numerical Cementation on Multiphase Displacement in Rough Fractures. *Transport in Porous Media*, 116(1):275–293.

[97] Tokunaga, T. K. and Wan, J. (2013). Capillary Pressure and Mineral Wettability Influences on Reservoir CO2 Capacity. *Reviews in Mineralogy and Geochemistry*, 77(1):481–503.

[98] Verma, R., Icardi, M., and Prodanović, M. (2018). Effect of wettability on two-phase quasi-static displacement: Validation of two pore scale modeling approaches. *Journal of Contaminant Hydrology*.

[99] Washburn, E. W. (1921). The Dynamics of Capillary Flow. *Physical Review*, 17(3):273–283.

[100] Wenzel, R. N. (1936). Resistance of solid surfaces to wetting by water. *Industrial & Engineering Chemistry*, 28(8):988–994.

[101] Wildenschild, D. and Sheppard, A. P. (2013). X-ray imaging and analysis techniques for quantifying pore-scale structure and processes in subsurface porous medium systems. *Advances in Water Resources*, 51:217–246.

[102] Witherspoon, P. A., Wang, J. S. Y., Iwai, K., and Gale, J. E. (1980). Validity of Cubic Law for fluid flow in a deformable rock fracture. *Water Resources Research*, 16(6):1016–1024.

[103] Wolansky, G. and Marmur, A. (1999a). Apparent contact angles on rough surfaces: The Wenzel equation revisited. *Colloids and Surfaces A: Physicochemical and Engineering Aspects*, 156(1-3):381–388.

[104] Wolansky, G. and Marmur, A. (1999b). Apparent contact angles on rough surfaces: the Wenzel equation revisited. *Colloids and Surfaces A: Physicochemical and Engineering Aspects*, 156(1-3):381–388.

[105] Wolfram, S. (1983). Statistical mechanics of cellular automata. *Reviews of Modern Physics*, 55(3):601–644.

[106] Zhang, J., Li, B., and Kwok, D. Y. (2009). Metastable contact angles and self-propelled drop movement on chemically heterogeneous surfaces by a mean-field lattice Boltzmann model. *European Physical Journal: Special Topics*, 171(1):73–79.

[107] Zimmerman, R. W., Al-Yaarubi, A., Pain, C. C., and Grattoni, C. A. (2004). Non-linear regimes of fluid flow in rock fractures. *International Journal of Rock Mechanics and Mining Sciences*, 41(SUPPL. 1):1–7.